SANDIA REPORT
SAND2014-16996
Unlimited Release
July 2014

Time-Resolved, Quantitative Measurement of OH, HO_2 and CH_2O in Fuel Oxidation Reactions by High Resolution IR Absorption Spectroscopy

Haifeng Huang, Brandon Rotavera and Craig A. Taatjes

Prepared by
Sandia National Laboratories
Albuquerque, New Mexico 87185 and Livermore, California 94550

Sandia National Laboratories is a multi-program laboratory managed and operated by Sandia Corporation, a wholly owned subsidiary of Lockheed Martin Corporation, for the U.S. Department of Energy's National Nuclear Security Administration under contract DE-AC04-94AL85000.

Issued by Sandia National Laboratories, operated for the United States Department of Energy by Sandia Corporation.

Available to DOE and DOE contractors from
U.S. Department of Energy
Office of Scientific and Technical Information
P.O. Box 62
Oak Ridge, TN 37831

Telephone: (865) 576-8401
Facsimile: (865) 576-5728
E-Mail: reports@adonis.osti.gov
Online ordering: http://www.osti.gov/bridge

Available to the public from
U.S. Department of Commerce
National Technical Information Service
5285 Port Royal Rd.
Springfield, VA 22161

Telephone: (800) 553-6847
Facsimile: (703) 605-6900
E-Mail: orders@ntis.fedworld.gov
Online order: http://www.ntis.gov/help/ordermethods.asp?loc=7-4-0#online

SAND2014-16996
Unlimited Release
July 2014

Time-Resolved, Quantitative Measurement of OH, HO_2 and CH_2O in Fuel Oxidation Reactions by High Resolution IR Absorption Spectroscopy

Haifeng Huang, Brandon Rotavera and Craig A. Taatjes

Combustion Chemistry Department, Combustion Research Facility,
Sandia National Laboratories, Livermore, CA 94550

Abstract

Combined with a Herriott-type multi-pass slow flow reactor, high-resolution differential direct absorption spectroscopy has been used to probe, *in situ* and quantitatively, hydroxyl (OH), hydroperoxy (HO_2) and formaldehyde (CH_2O) molecules in fuel oxidation reactions in the reactor, with a time resolution of about 1 micro-second. While OH and CH_2O are probed in the mid-infrared (MIR) region near 2870nm and 3574nm respectively, HO_2 can be probed in both regions: near-infrared (NIR) at 1509nm and MIR at 2870nm. Typical sensitivities are on the order of 10^{10} – 10^{11} molecule cm^{-3} for OH at 2870nm, 10^{11} molecule cm^{-3} for HO_2 at 1509nm, and 10^{11} molecule cm^{-3} for CH_2O at 3574nm. Measurements of multiple important intermediates (OH and HO_2) and product (CH_2O) facilitate to understand and further validate chemical mechanisms of fuel oxidation chemistry.

ACKNOWLEDGMENTS

This material is based upon work supported by the U.S. Department of Energy, Office of Science, Office of Basic Energy Sciences (BES). The authors want to thank Howard Johnsen, Kendrew Au, Erxiong Huang, Brian Patterson, Chris Carlen and Paul Fugazzi for great technical help.

CONTENTS

FIGURES

TABLES

1. Introduction

Low-temperature hydrocarbon fuel oxidation process is complex. It happens through a reaction network involving a large number of species [1]. For example, one detailed chemical kinetics model of a C4 fuel molecule, *n*-butane, includes 176 different species and 1111 reactions [2]. On the other hand, low temperature autoignition chemistry [3] is critical to the development of next-generation internal combustion engines, e.g. HCCI engine [4] in which ignition timing is controlled solely by the autoignition chemistry of fuel molecules. The general scheme of low temperature hydrocarbon oxidation and autoignition chemistry [3] is summarized in Figure 1.

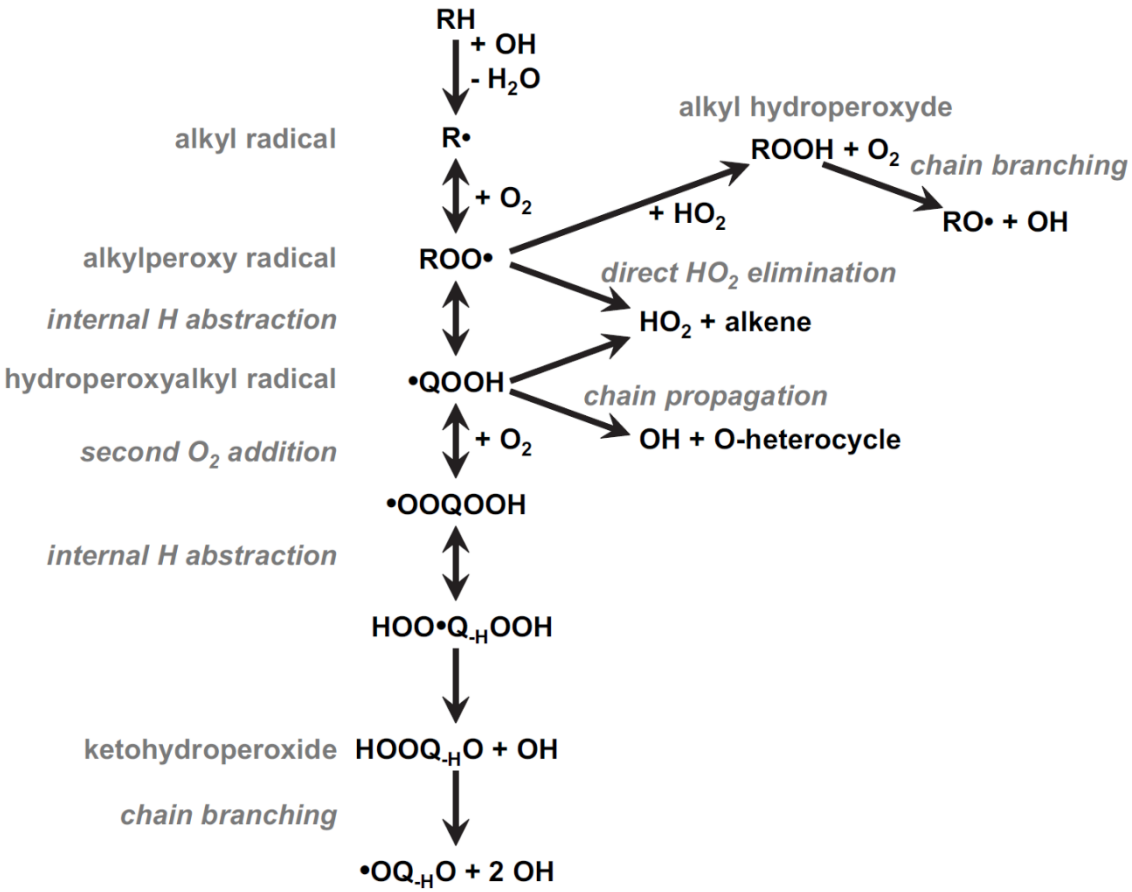

Figure 1. Schematic mechanism for low-temperature hydrocarbon oxidation and autoignition chemistry [3]

Because of the importance, scientists have spent tremendous efforts to understand the detailed chemical mechanisms of fuel autoignition both experimentally and theoretically. While detailed chemical mechanisms can be developed by powerful quantum chemistry calculations,

quantitative measurements of transient time profiles of important intermediates and products in fuel oxidation reactions are fundamental in both exploring and further validating those chemical mechanisms. In the laser chemistry lab at Combustion Research Facility at Sandia, we use laser flash photolysis [5, 6], slow flow reactor to study low-temperature (< 800K) and low-pressure (< 100Torr) fuel oxidation chemistry [7]. High-resolution IR spectroscopic tools have been used to probe the time behavior of important intermediates and products in fuel oxidation reactions *in situ*.

In hydrocarbon fuel oxidation chemistry, one of the most important molecules is hydroxyl (OH) radical because it is the major chain propagator in fuel-oxidation process [1, 3]. Previously [8], we have probed trace OH in the reactor by using the strong X→A electronic transitions near 308nm [9]. The OH absorption lines in this region are well separated, with minimal interference, and have very large absorption cross-sections (on the order of 10^{-16} cm^2) [9]. These lines are widely used in OH detection. In our lab, the OH detection limit using a continuous wave (cw) 308nm uv laser is on the order of 10^9 molecule cm^{-3} or even better.

Although the sensitivity is high when probing OH at 308nm, the uv probe laser can cause unwanted side reactions, which makes it very hard to quantitatively simulate recorded data. In our experiments, either molecular chlorine (Cl_2) [10] or oxalyl chloride (OxCl) [11] is used as the initial radical precursor by photolysis of them with 355nm or 266nm laser respectively. On the other hand, both Cl_2 and OxCl absorb 308nm light with significant cross sections (2×10^{-19} cm^2 for Cl_2 and 7×10^{-20} cm^2 for OxCl) [10, 11], which will generate a reaction background in the column of gas defined by the diameter of the probe uv laser beam before photolysis pulses arrive. When the studied chemistry is triggered by a photolysis pulse, the pre-existing reaction background, which includes a distribution of radicals and products, will be entangled with the studied chemistry. Although diffusion process can reduce the interference from the background reactions, this entanglement makes data simulation complicated because of the difficulty in determining the initial reaction conditions at the time spot of photolysis trigger. More importantly, several very important intermediates in fuel oxidation chemistry such as alkylperoxy (RO_2) [12], OOQOOH (hydroperoxyalkyl radical QOOH after second O_2 addition) absorb 308nm light, which will dissociate them and possibly change their chemistry. Some fuel

molecules, such as *tert*-butyl hydroperoxide (TBHP), have small absorption cross-section at 308nm (about 2×10^{-21} cm^2) which can dissociate the fuel molecule [13]. One apparent solution for the above difficulties is to use a cw 308nm probe laser as weak as possible, e.g. less than 0.5mW. In this way, the side effects caused by the probe laser can be reduced down to an unimportant level. Such low power leads to a technical disadvantage, making laser alignment in a multi-pass configuration difficult.

To avoid all the above issues, we have adopted another solution: use a MIR cw laser to probe OH radical with its vibrational fundamental transitions [14]. The laser source we used is our narrow linewidth (< 50 kHz) cw-OPO laser system (LINOS OS4000). The absorption cross-section of OH in this region is around 10^{-18} cm^2, two orders of magnitude less than that in the uv region. The sensitivity realized in this configuration is on the order of $10^{10} – 10^{11}$ molecule cm^{-3}, meeting the detection limit requirement for the studies on most combustion-relevant fuel molecules. The advantages of probing interesting intermediates in the MIR region are multifaceted. First, a MIR laser is non-intrusive when compared with a uv laser due to the lower photon energy and avoidance of electronic excitation. Second, many organic molecules have "fingerprint" absorption features in the MIR region [14], making it possible to probe multiple species in fuel oxidation reactions by a single cw-OPO laser. Third, our cw-OPO is much more user friendly than our 308nm uv laser, which is obtained from frequency doubling of a cw ring dye laser (Coherent 699).

Hydroperoxy (HO_2) radical generation is a chain-termination step in low-temperature autoignition chemistry (see Figure 1), which is a very important indicator of autoignition property of specific fuel molecules. In our laser chemistry lab, sensitive HO_2 detection based on two-tone frequency modulation (FM) spectroscopy in the NIR region [15] has been developed many years ago. The purpose of using FM spectroscopy is to remove the interference of thermal lensing noise from chemical reactions from the HO_2 absorption signal. In our recent experiments, we have found that thermal lensing noise and other common noise in data traces are greatly removed by subtracting an off absorption peak trace from an on-peak absorption time signal (see below for more details). Therefore, we have changed the detection method from two-tone FM to differential direct absorption spectroscopy, which reduces the complexity of our apparatus. The

absorption transitions we have used for HO_2 probe include: X→A electronic transitions near 1429nm [16], first overtone transitions of OH stretch ($2\nu_1$ band) at 1509nm [17, 18], and fundamental transitions of OH stretch (ν_1 band) at 2870nm [14]. For HO_2 molecule, the strong transitions in all three regions have similar line intensity. The two NIR regions can be reached by our external cavity diode laser (ECDL, New Focus, Velocity), and the cw-OPO laser can reach the ν_1 band of HO_2. Because the ECDL is much easier to use than the cw-OPO laser, we probe HO_2 molecule at 1509nm.

Another interesting molecule is formaldehyde (CH_2O). In low-temperature autoignition chemistry, it is a signature product of some important reaction channels [19-21]. The high resolution IR spectrum of CH_2O is well known [22]. We probe CH_2O molecule at the wavelength of 3574nm.

For OH detection, the line intensity [23-25] and pressure broadening coefficients by helium or oxygen [26] of the probed transition have been measured accurately . However, this is not the case for HO_2 and CH_2O detection. Fortunately, methanol (CH_3OH) oxidation system is a perfect reference system [15] for both HO_2 and CH_2O because it has a conversion efficiency from initial radical, i.e. Cl atom, to HO_2 (or CH_2O) very close to one through reactions:

$$Cl + CH_3OH \rightarrow CH_2OH + HCl \quad \text{(R1)}$$

$$CH_2OH + O_2 \rightarrow HO_2 + CH_2O \quad \text{(R2)}$$

From (R2) reaction we can see the yield of HO_2 is the same as CH_2O. Therefore, in our experiments, the measured HO_2 or CH_2O signal is normalized to that of the methanol oxidation system.

2. Details of the Experimental Setup

Figure 2 is a schematic diagram of our setup. Many details about this temperature controllable, slow laminar flow reactor can be found in previous publications from this group [15, 27]. The Cl-initialed oxidation chemistry in the gas mixture of fuel/O_2/buffer helium/Cl_2 (or OxCl) is triggered by either 355nm or 266nm photolysis laser pulse which passes the center line of the reactor. The photolysis laser is first collimated and expanded by a telescope, and then shaped down to 13mm diameter by an iris before it enters the cell. The probe IR laser beam is coupled to the reactor in off-axis angle and makes a Herriott-type multi-pass configuration [28] by using two spherical mirrors in the reactor, which has a near concentric design. The total number of passes is 25. The cylindrical photolysis column, within which the chemical reactions occur, intersects with the multi-pass probe laser beam near the center of the reactor. The absorption length of probed intermediates is defined as the total length of the probe laser beam overlapping with the photolysis column. Typical absorption length is about 15m.

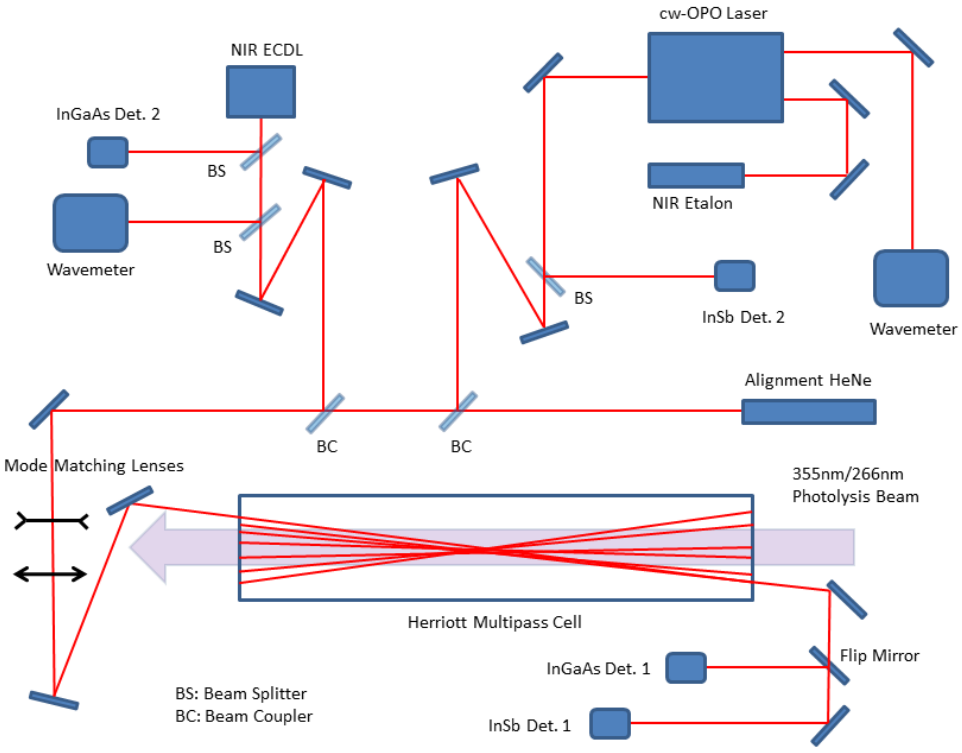

Figure 2. Schematic diagram of the experimental setup

A HeNe laser is used to alignment both IR lasers. After two different beam combiners, both NIR and MIR probe laser beams overlap with the HeNe laser beam very well in a distance of more than 5 meters, which makes the divergence between the two IR probe laser beams and the HeNe negligible even after long distance (150cm × 25) travel in the multi-pass cell. Figure 3 is a picture of the setup.

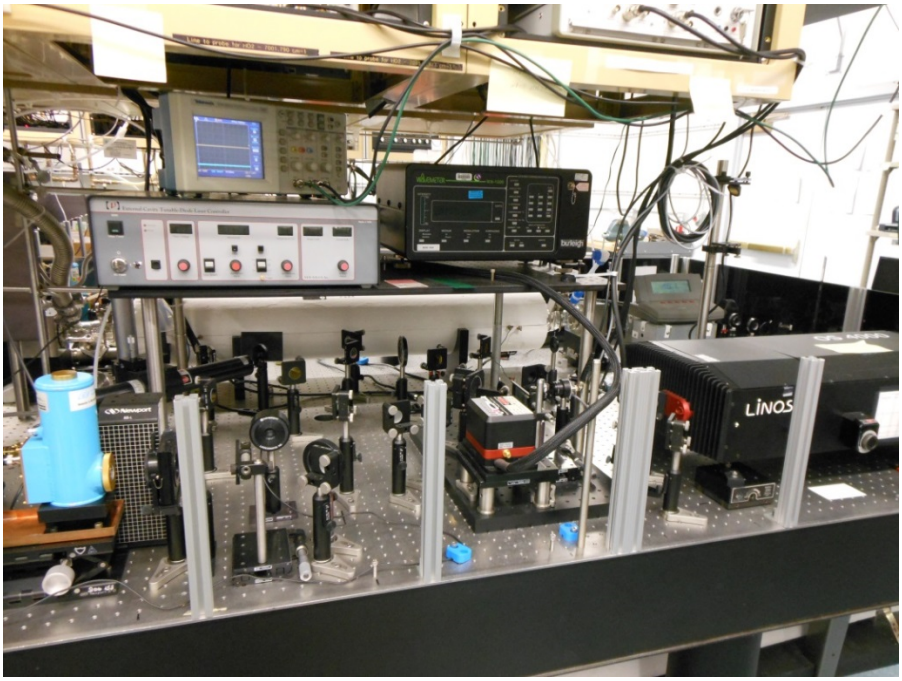

Figure 3. Picture of the setup. The white horizontal column in the back is the temperature controllable flow reactor.

Both probe lasers are coupled to the Herriott multi-pass cell [28] after mode matching. After the NIR ECDL output, two beam splitters are used to extract two new beams. One is detected by an InGaAs photodiode and the signal is used as the reference for the differential absorption measurement. A continuously adjustable neutral density attenuator is used to control this reference signal level. The other laser beam is directed to a wavemeter (Burleigh WA-1500) for simultaneous monitoring of the laser wavelength. The cw-OPO laser has two idler beam outputs. One is used as the probe laser beam and the other is coupled to another Burleigh WA-1500 wavemeter for wavelength monitoring. The signal beam (NIR) of the cw-OPO is coupled to a NIR etalon which has a free spectral range (FSR) of 1.5GHz and a resolution of about 10MHz. Figure 4 is a picture of the NIR etalon. The purpose of the etalon is to monitor if the cw-OPO

runs at single longitudinal mode. If the cw-OPO runs at multiple mode conditions, first, the laser intensity will be very noisy because of mode competition; second, the measured absorption signal will not reflect true chemistry because different laser modes probe different parts of the absorption features. Similar to the NIR ECDL, a reference beam is extracted by a beam splitter and measured by a liquid-nitrogen-cooled InSb detector. The reference signal level is controlled by another continuously adjustable attenuator.

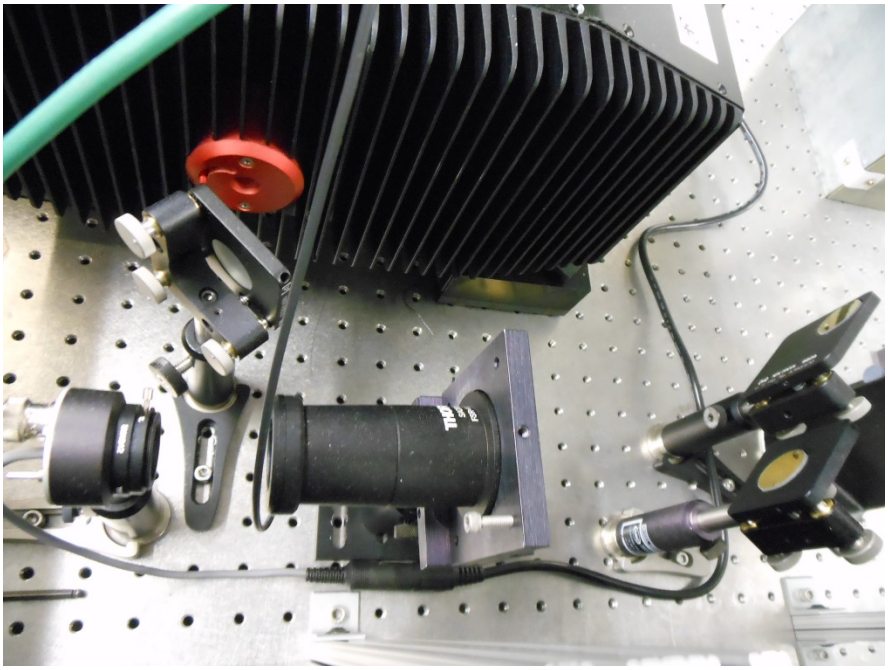

Figure 4. NIR etalon used to monitor single mode running of the cw-OPO laser

Figure 5 is a picture of the optics after the output of the Herriott cell. After the output of the Herriott cell, the two probe lasers beam are detected by one InGaAs photodiode and another liquid-nitrogen-cooled InSb detector respectively. A flip mirror is used to direct the NIR probe beam to the InGaAs detector if HO_2 is measured. When OH or CH_2O are measured, the flip mirror will be put down. A continuous turning wheel attenuator is used to adjust the signal level of both detectors. In measurements, the detector signal containing absorption information, either NIR or MIR, and the corresponding reference signal are connected to the two inputs of a differential amplifier (SRS SR560) for the amplification of absorption signal.

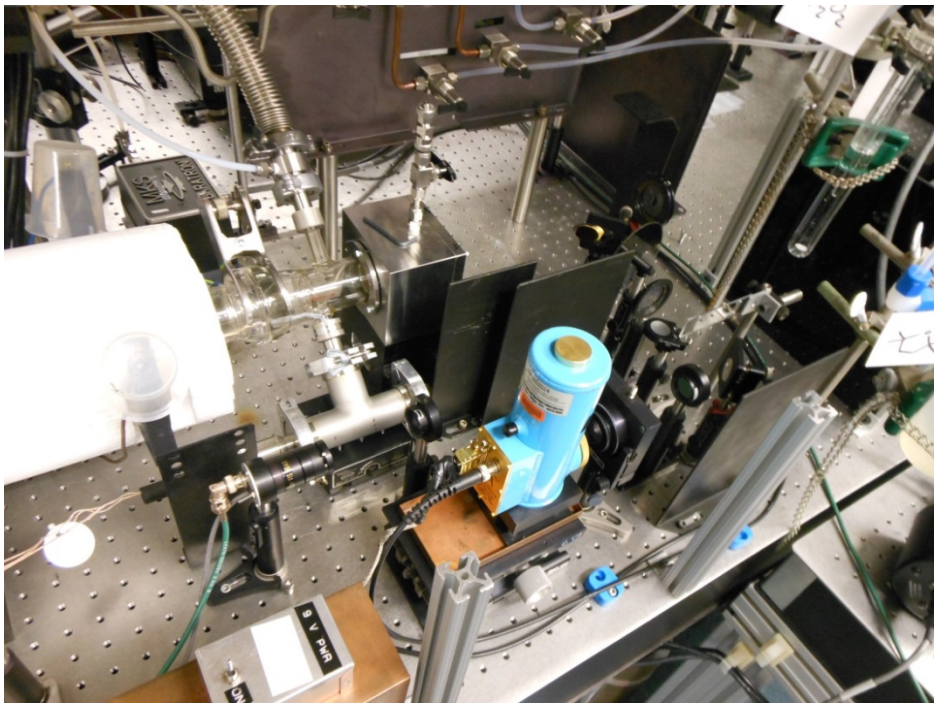

Figure 5. Detection zone after the output of the Herriott cell

3. Mass Flow Controller (MFC) Calibration

In our measurements, we want the initial concentrations of different gas components in the reactor as accurate as possible. We use calibrated mass flow controllers (MFC) to control the flow rates of different gas flows such as buffer helium, oxygen, helium for fuel bubbler, pure fuel gases, helium for methanol bubbler and helium for OxCl bubbler. We have found that the calibration of MFCs by the manufacturer only lasts certain period of time, e.g. 1 year or less, after which the gas correction factor of a MFC drifts away from calibrated values. We have also found that the drifted gas correction factor of a MFC is stable for very long time (several years) when it is fully warmed up and no adjustments such as zero point or servo loop gain have been made. As one can see from the plots below, even for a freshly calibrated MFC, its gas correction factor is substantially off from the normal value if the flow rate is set below 1/10 of its full scale range. However, our measurements often need a broad range of gas flow rates with a single MFC. For all those, we have developed a new method of MFC calibration which leads to calibrations stable for years.

We use a freshly calibrated MFC for oxygen flow as the standard. Its full scale flow rate is 1000sccm. The gas correction factor for oxygen is 0.993, very close to 1.0 (MKS Instruments). We found this gas correction factor is very stable in the range from 500sccm to 900sccm. In out calibration process, we first pumped down the cell. Then we set a flow rate in the above range with pure oxygen flow. What we measured is the pressure increase in the cell in a certain period of time, e.g. 5 min. Then we calculated the cell pressure increase in unit time and of unit flow rate. We have performed this measurement many times during several years and the results are very close to the value 0.18 Torr/min/sccm. If we assume the gas factor 0.993 is correct, then the total volume of the reactor (including the tubing volume) is $760 \times 0.993 / 0.18 = 4193$ cm^3. We have measured this pressure increase per unit time and unit sccm for all MFCs in a very broad range of flow rates and scaled this pressure increase to the stable value 0.18 Torr/min/sccm of oxygen. This ratio is equal to the gas correction factor of specific flow conditions (specific MFC, flow rate setting and gas type) if we approximate the gas factor of oxygen to be 1.0. Figure 6 is a calibration for buffer helium flow. The MFC has a full scale flow of 5000sccm. As shown in the plot, the gas correction factor for flows below 1000sccm setting is much larger than 1.52 at large flows. We have fitted the measured gas correction factors to the equation 1.52 + 369/x -1.08E-5

x with x the flow rate setting. The fractional error of the fitting in the whole range is less than ± 5%, as shown in the upper right corner of Figure 6. Similar calibrations for other MFCs are summarized in Appendix A.

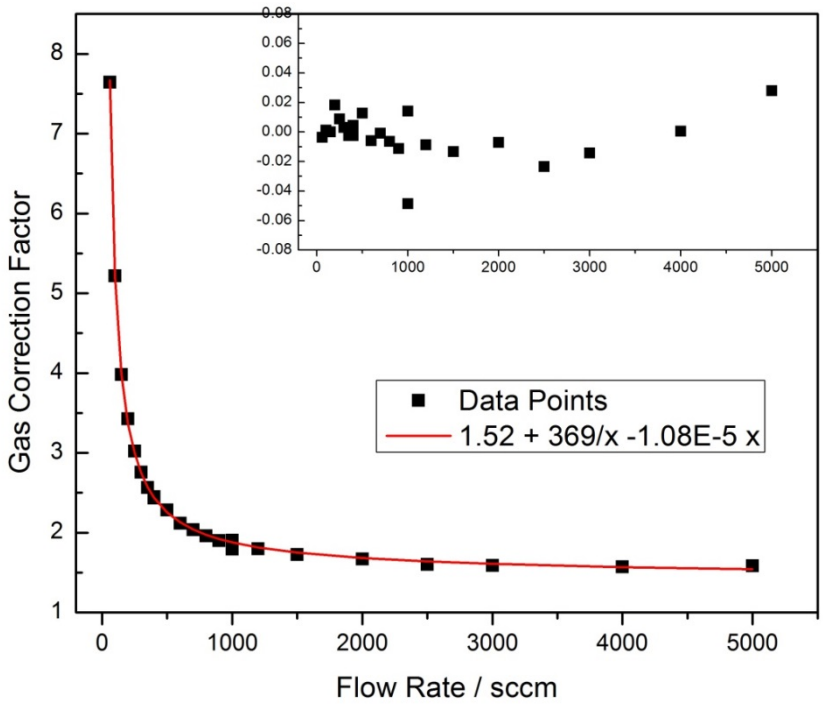

Figure 6. Gas correction factor calibration of a 5000sccm MFC for buffer helium gas flow

Table 1 summarizes the calibrations for different MFCs. We have tested how accurate this calibration method by measuring the concentration of Cl_2 in the reactor with the cw 308nm uv laser. The absorption cross section of Cl_2 at 308nm has been determined acuurately [10]. The measured Cl_2 concentration agrees with the calculated one from flow conditions to accuracy of 5-10%.

The fitted polynomials are used in the Excel worksheet for the design of experimental conditions. Figure 7-1 is the worksheet part for designing the initial concentrations of different gases. With all the fitted polynomials, it is very convenient to change flow rates to reach the preferred initial concentrations. With designed flow rates, the photolysis rate is set to a value with which the reactor has enough time to be refreshed totally when next photolysis pulse

arrives. Figure 7-2 is an image of the worksheet part calculating the peak absorption cross section of OH, which will be explained in detail in next section.

Table 1. Summary of calibrations of gas correction factor for different MFCs

Gas Lines	MFC Full Scale (sccm)	Calibrated Flow Range (sccm)	Gas Correction Factor Calibration	Precision and Note
Buffer helium	5000	60 - 4999	1.52 + 369/x - 1.08E-5 x	+/- 3%
Fuel bubbler helium	2000	80 - 1500	1.44 - 49.5/x + 1.19E-5 x	+/- 4%
OxCl bubbler helium	20	4 – 19.9	1.24 + 9.58E-2/x -1.84E-3 x	+/- 1%
CH_3OH bubbler helium	500	5 - 400	1.44 + 0.805/x - 2.60E-4 x	+/- 3%
5% Cl_2 in helium	100	5 - 99	1.40 + 5.42/x - 1.19E-3 x	+/- 1%
Oxygen	1000	10 - 999	1.01 + 14.9/x - 5.67E-5 x	+/- 4% Not for zero O_2
Propane	50	10 - 49	0.352 – 0.321/x + 8.19E-5 x	+/- 1%

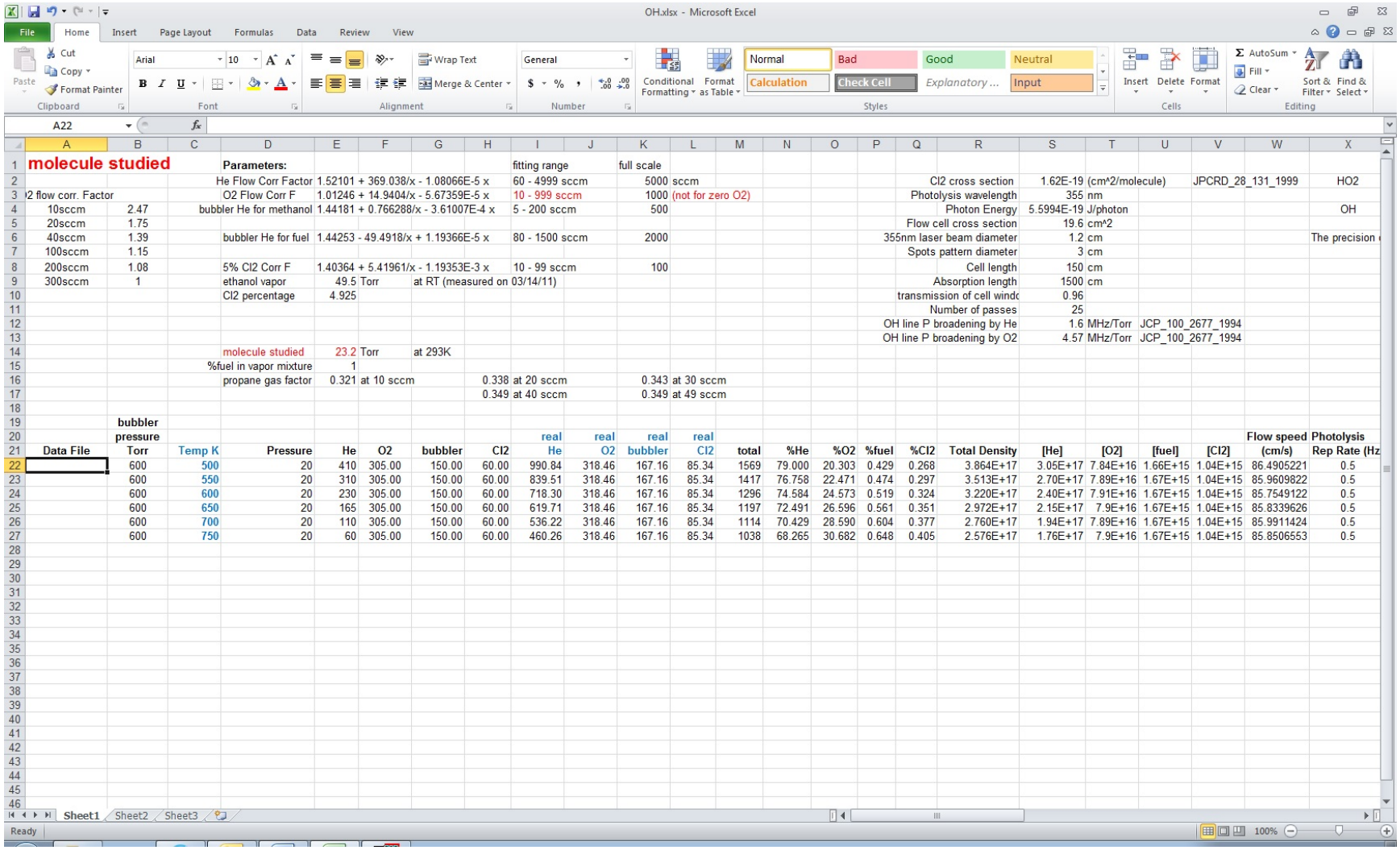

OH.xlsx - Microsoft Excel

	A	B	C	D	E	F	G	H	I	J	K	L	M	N	O	P	Q	R	S	T	U	V	W	X
1	**molecule studied**			**Parameters:**					fitting range		full scale													
2				He Flow Corr Factor	1.52101 + 369.038/x - 1.08066E-5 x				60 - 4999 sccm		5000	sccm						Cl2 cross section	1.62E-19	(cm^2/molecule)		JPCRD_28_131_1999		HO2
3	)2 flow corr. Factor			O2 Flow Corr F	1.01246 + 14.9404/x - 5.67359E-5 x				10 - 999 sccm		1000	(not for zero O2)						Photolysis wavelength	355	nm				
4	10sccm	2.47		bubbler He for methanol	1.44181 + 0.766288/x - 3.61007E-4 x				5 - 200 sccm		500							Photon Energy	5.5994E-19	J/photon				OH
5	20sccm	1.75																Flow cell cross section	19.6	cm^2				
6	40sccm	1.39		bubbler He for fuel	1.44253 - 49.4918/x + 1.19366E-5 x				80 - 1500 sccm		2000							355nm laser beam diameter	1.2	cm				The precision
7	100sccm	1.15																Spots pattern diameter	3	cm				
8	200sccm	1.08		5% Cl2 Corr F	1.40364 + 5.41961/x - 1.19353E-3 x				10 - 99 sccm		100							Cell length	150	cm				
9	300sccm	1		ethanol vapor	49.5	Torr	at RT (measured on	03/14/11)										Absorption length	1500	cm				
10				Cl2 percentage	4.925													transmission of cell windo	0.96					
11																		Number of passes	25					
12																		OH line P broadening by He	1.6	MHz/Torr	JCP_100_2677_1994			
13																		OH line P broadening by O2	4.57	MHz/Torr	JCP_100_2677_1994			
14				molecule studied	23.2	Torr	at 293K																	
15				%fuel in vapor mixture	1																			
16				propane gas factor	0.321	at 10 sccm		0.338	at 20 sccm		0.343	at 30 sccm												
17								0.349	at 40 sccm		0.349	at 49 sccm												
18																								
19		bubbler																						
20		pressure							real	real	real	real											Flow speed	Photolysis
21	Data File	Torr	Temp K	Pressure	He	O2	bubbler	Cl2	He	O2	bubbler	Cl2	total	%He	%O2	%fuel	%Cl2	Total Density	[He]	[O2]	[fuel]	[Cl2]	(cm/s)	Rep Rate (Hz
22		600	500	20	410	305.00	150.00	60.00	990.84	318.46	167.16	85.34	1569	79.000	20.303	0.429	0.268	3.864E+17	3.05E+17	7.84E+16	1.66E+15	1.04E+15	86.4905221	0.5
23		600	550	20	310	305.00	150.00	60.00	839.51	318.46	167.16	85.34	1417	76.758	22.471	0.474	0.297	3.513E+17	2.70E+17	7.89E+16	1.67E+15	1.04E+15	85.9609822	0.5
24		600	600	20	230	305.00	150.00	60.00	718.30	318.46	167.16	85.34	1296	74.584	24.573	0.519	0.324	3.220E+17	2.40E+17	7.91E+16	1.67E+15	1.04E+15	85.7549122	0.5
25		600	650	20	165	305.00	150.00	60.00	619.71	318.46	167.16	85.34	1197	72.491	26.596	0.561	0.351	2.972E+17	2.15E+17	7.9E+16	1.67E+15	1.04E+15	85.8339626	0.5
26		600	700	20	110	305.00	150.00	60.00	536.22	318.46	167.16	85.34	1114	70.429	28.590	0.604	0.377	2.760E+17	1.94E+17	7.89E+16	1.67E+15	1.04E+15	85.9911424	0.5
27		600	750	20	60	305.00	150.00	60.00	460.26	318.46	167.16	85.34	1038	68.265	30.682	0.648	0.405	2.576E+17	1.76E+17	7.9E+16	1.67E+15	1.04E+15	85.8506553	0.5

Sheet1 Sheet2 Sheet3

Ready

Figure 7-1. Excel worksheet for designing experimental conditions in OH measurement

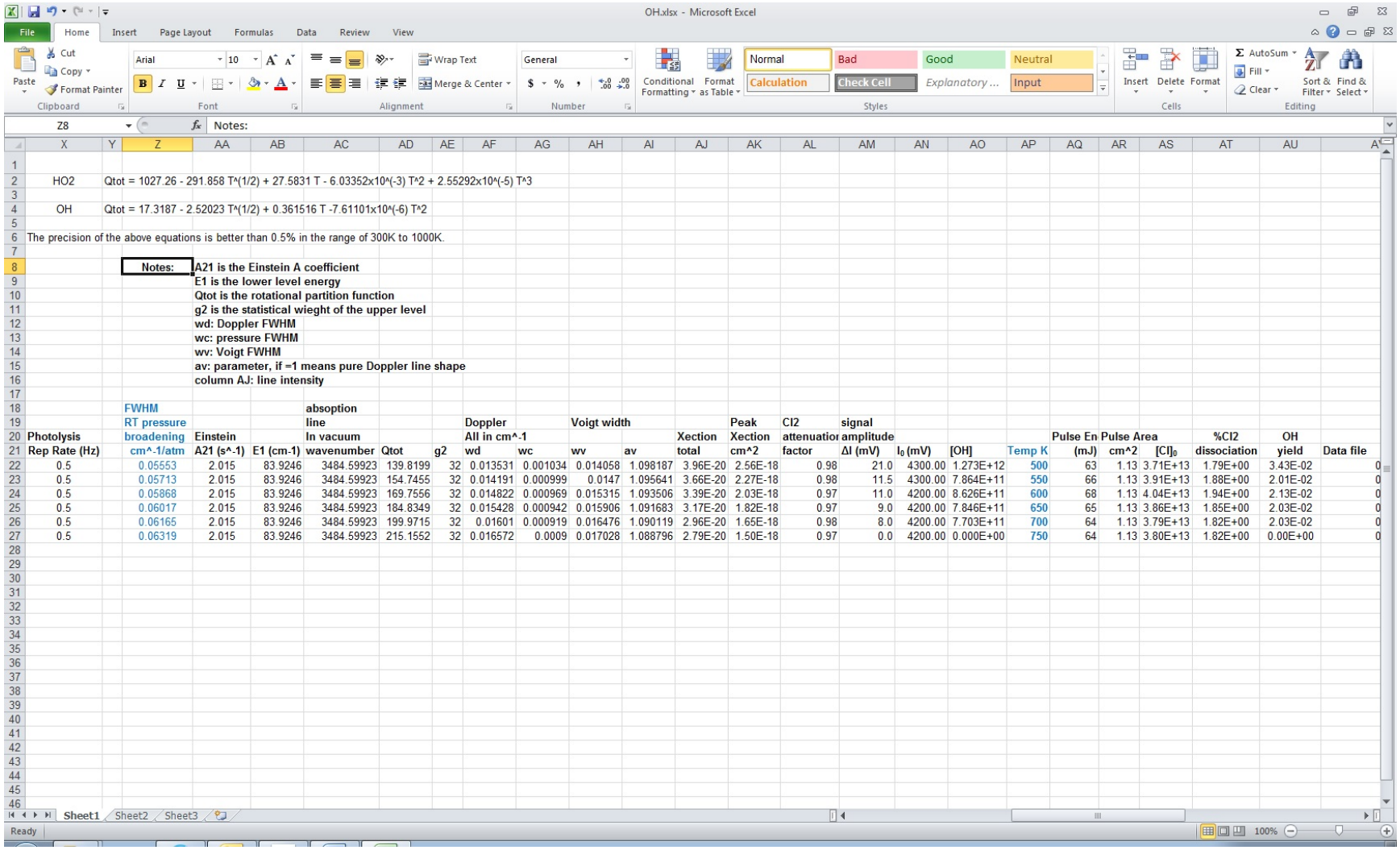

OH.xlsx - Microsoft Excel

1																											
2	HO2	Qtot = 1027.26 - 291.858 T^(1/2) + 27.5831 T - 6.03352x10^(-3) T^2 + 2.55292x10^(-5) T^3																									
3																											
4	OH	Qtot = 17.3187 - 2.52023 T^(1/2) + 0.361516 T -7.61101x10^(-6) T^2																									
5																											
6	The precision of the above equations is better than 0.5% in the range of 300K to 1000K.																										
7																											
8		Notes:	A21 is the Einstein A coefficient																								
9			E1 is the lower level energy																								
10			Qtot is the rotational partition function																								
11			g2 is the statistical wieght of the upper level																								
12			wd: Doppler FWHM																								
13			wc: pressure FWHM																								
14			wv: Voigt FWHM																								
15			av: parameter, if =1 means pure Doppler line shape																								
16			column AJ: line intensity																								
17																											
18		FWHM			absoption																						
19		RT pressure			line			Doppler		Voigt width			Peak	CI2	signal												
20	Photolysis	broadening	Einstein		In vacuum			All in cm^-1				Xection	Xection	attenuation	amplitude				Pulse En	Pulse Area		%CI2	OH			
21	Rep Rate (Hz)	cm^-1/atm	A21 (s^-1)	E1 (cm-1)	wavenumber	Qtot	g2	wd	wc	wv	av	total	cm^2	factor	Δl (mV)	I_0 (mV)	[OH]	Temp K	(mJ)	cm^2	$[Cl]_0$	dissociation	yield	Data file			
22	0.5	0.05553	2.015	83.9246	3484.59923	139.8199	32	0.013531	0.001034	0.014058	1.098187	3.96E-20	2.56E-18	0.98	21.0	4300.00	1.273E+12	500	63	1.13	3.71E+13	1.79E+00	3.43E-02	0			
23	0.5	0.05713	2.015	83.9246	3484.59923	154.7455	32	0.014191	0.000999	0.0147	1.095641	3.66E-20	2.27E-18	0.98	11.5	4300.00	7.864E+11	550	66	1.13	3.91E+13	1.88E+00	2.01E-02	0			
24	0.5	0.05868	2.015	83.9246	3484.59923	169.7556	32	0.014822	0.000969	0.015315	1.093506	3.39E-20	2.03E-18	0.97	11.0	4200.00	8.626E+11	600	68	1.13	4.04E+13	1.94E+00	2.13E-02	0			
25	0.5	0.06017	2.015	83.9246	3484.59923	184.8349	32	0.015428	0.000942	0.015906	1.091683	3.17E-20	1.82E-18	0.97	9.0	4200.00	7.846E+11	650	65	1.13	3.86E+13	1.85E+00	2.03E-02	0			
26	0.5	0.06165	2.015	83.9246	3484.59923	199.9715	32	0.01601	0.000919	0.016476	1.090119	2.96E-20	1.65E-18	0.98	8.0	4200.00	7.703E+11	700	64	1.13	3.79E+13	1.82E+00	2.03E-02	0			
27	0.5	0.06319	2.015	83.9246	3484.59923	215.1552	32	0.016572	0.0009	0.017028	1.088796	2.79E-20	1.50E-18	0.97	0.0	4200.00	0.000E+00	750	64	1.13	3.80E+13	1.82E+00	0.00E+00	0			
28																											
29																											
30																											
31																											
32																											
33																											
34																											
35																											
36																											
37																											
38																											
39																											
40																											
41																											
42																											
43																											
44																											
45																											
46																											

Sheet1 Sheet2 Sheet3

Ready

Figure 7-2. Excel worksheet for calculating the peak absorption cross section of OH

4. OH Measurement

The OH lines we selected are $P(2.5)1^+$ and $P(2.5)1^-$ pair of OH fundamental transitions at 3484.74918cm^{-1} and 3484.59923cm^{-1} respectively [14, 23]. Our WA-1500 wavemeter has a small deviation of 0.005cm^{-1}, making the measured wavenumbers of the two lines to be 3484.744cm^{-1} and 3484.595cm^{-1}. Figure 8 is a spectrum of the two lines from literature.

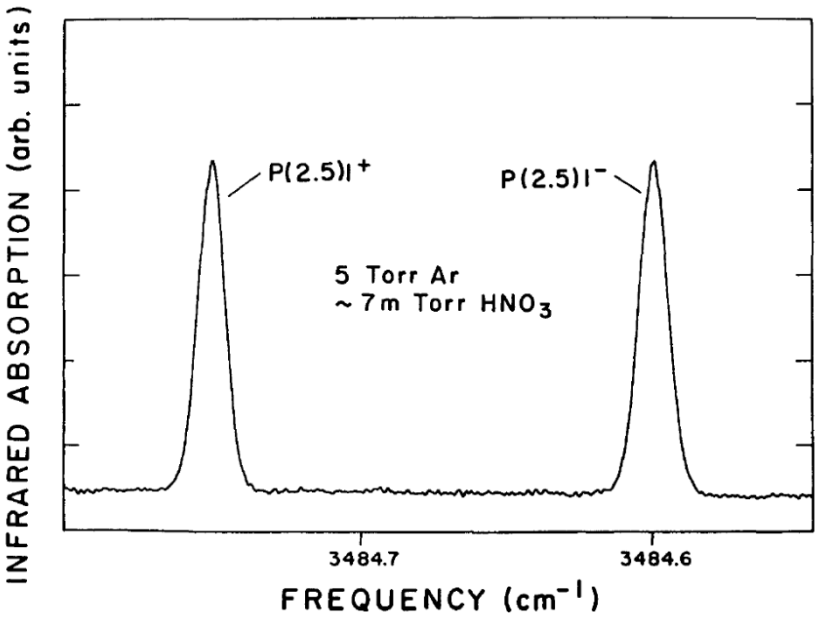

Figure 8. OH line pair $P(2.5)1^+$ and $P(2.5)1^-$ [23]

For the two OH absorption lines we selected, both the line intensities and pressure broadening coefficients by helium and oxygen at room temperature have been carefully measured by Nesbitt and his coworkers [23-26]. In order to calculate the peak absorption cross-section of OH at different temperatures (from 296K to 1000K), we have adopted their line intensities, the assignments of the two lines and the rotational partition function calculation of HITRAN database[14]. The temperature-dependence exponent under our experiments (helium buffer gas) is approximated by that of air from HITRAN, i.e. 0.66. This approximation only has minor effect on the OH peak absorption cross section because the OH lines are mainly Doppler broadened under our low pressure experimental conditions (typically less than 30Torr). We use Voigt line profile for the absorption cross section calculation. For simplicity, we used the approximation proposed by Whiting for the line profile calculation [9], which agrees with Voigt profile within

5% at worst. Figure 7-2 is the Excel worksheet used to calculate the OH absorption cross section. The rotational partition function values from HITRAN have been fitted to a function of temperature T with a precision of better than 0.5% in the range from 296K to 1000K. Definitions of the related parameters can be found in Figure 7-2.

In OH measurements, the probe cw-OPO laser wavelength is scanned near the OH lines. Besides the time trace with the laser wavelength tuned on OH peak of the absorption line, several time traces off OH peak will also be recorded at different wavelengths. Then the on-peak trace will be subtracted by one of the off-peak traces. The purpose of doing this is twofold. Very often, the OH lines are on top of a small but broad absorption or depletion background signal near 3484.6cm^{-1}, possibly caused by absorptions from new species generated in chemical reactions or from fuel molecule. By multiple off-peak measurements (off by several Voigt linewidth), we can determine the behavior of this background and remove it from the OH absorption signal. For all the oxidation systems we have studied, we did not observe very large background absorption/depletion near these two OH absorption lines.

Second, when chemical reactions are triggered by photolysis laser pulses, both the temperature and pressure in the reaction column will change because of energy release and species components change from chemical reactions, which will cause the refractive index fluctuation in the reaction zone. This fluctuation will cause the so-called thermal lensing noise in the measured signal [29]. Interestingly, we found that the above background subtraction process removes almost all the thermal lensing noise. Included in Appendix C are two programs written in Mathematica for this background subtraction data processing, one for OH and the other for HO_2. Both programs contain detailed notes. One can see from both two examples that this process works very well for thermal lensing noise reduction. Previously, this noise was removed by using frequency modulation (FM) method. The above background subtraction idea gives another simpler way of solving this difficulty. When the total time window of measurement is set to more than 10ms, the effectiveness of this background subtraction will slightly decrease. Different oxidation systems show different level of thermal lensing noise.
Figure 9 gives one example of this background subtraction data processing. After the background subtraction step, measured OH signal (in volt) will be converted into OH concentration time

profile by using Beer's law with measured laser intensity of no OH absorption (in volt), calculated OH absorption cross-section, and the absorption length determined based on the geometry of the multi-pass alignment. Figure 10 is the OH concentration traces at different temperatures in 1-butanol oxidation measured by the above method. OxCl was used as the initial Cl atom source.

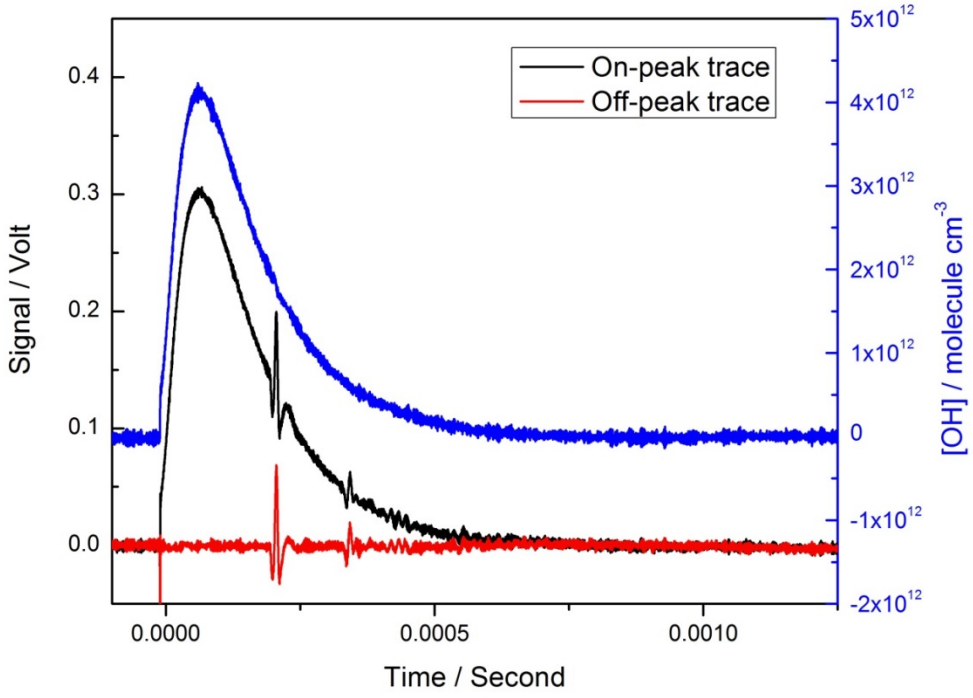

Figure 9. OH on-peak time trace subtracted by an off-peak trace. The differential trace (blue) has less noise and has been shifted upward for clarity.

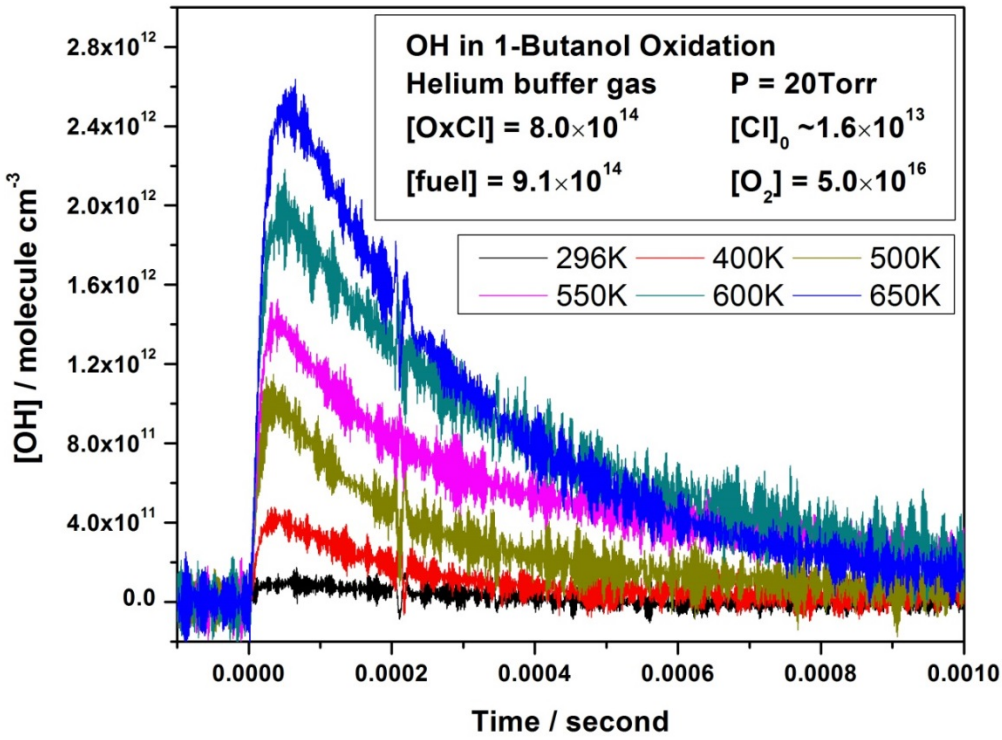

Figure 10. OH concentration time profiles at different temperatures in 1-butanol oxidation

The measured OH concentration time profiles are normalized to the initial Cl atom concentrations, giving time profiles of OH yields, especially peak OH yields. Figures 11 and 12 show the measured peak OH yields vs. O_2 concentration at different temperatures in the reacting system TBHP/O_2/Cl_2/355nm with helium buffer gas, and Figures 13 and 14 display the results of similar experiments in the reacting system helium/TBHP/O_2/OxCl/355nm. Here TBHP is used as the precursor of QOOH radicals by the reaction TBHP + Cl [30]. As one can see from the plots, the behavior of peak OH yield differs substantially between using Cl_2 and OxCl, especially when the flow cell temperature is above 480K. Figure 15 is a comparison plot of the peak OH yield vs. O_2 at 550K between two Cl precursors. With zero oxygen, the yield with Cl_2 is much lower than that with OxCl, suggesting more experiments are needed in order to clarify this puzzle.

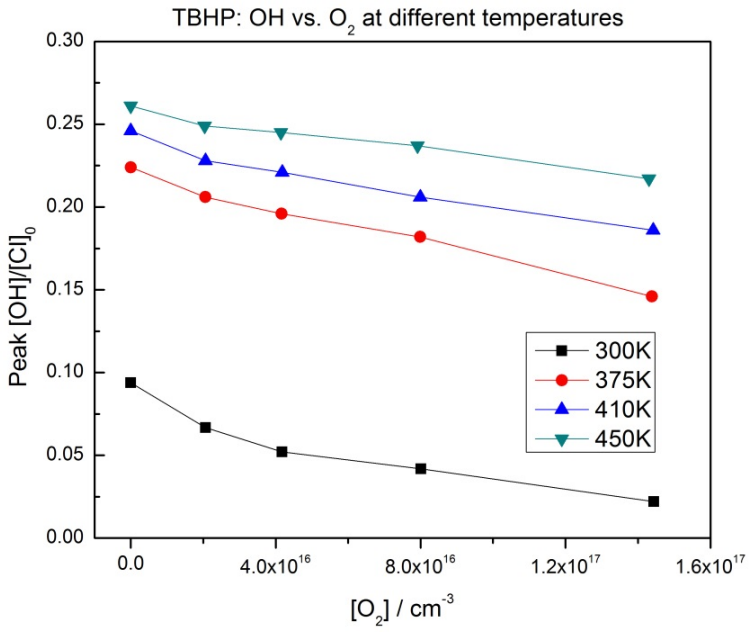

Figure 11. Peak OH yield vs. [O_2] between 300K and 450K in helium/TBHP/Cl_2/355nm system

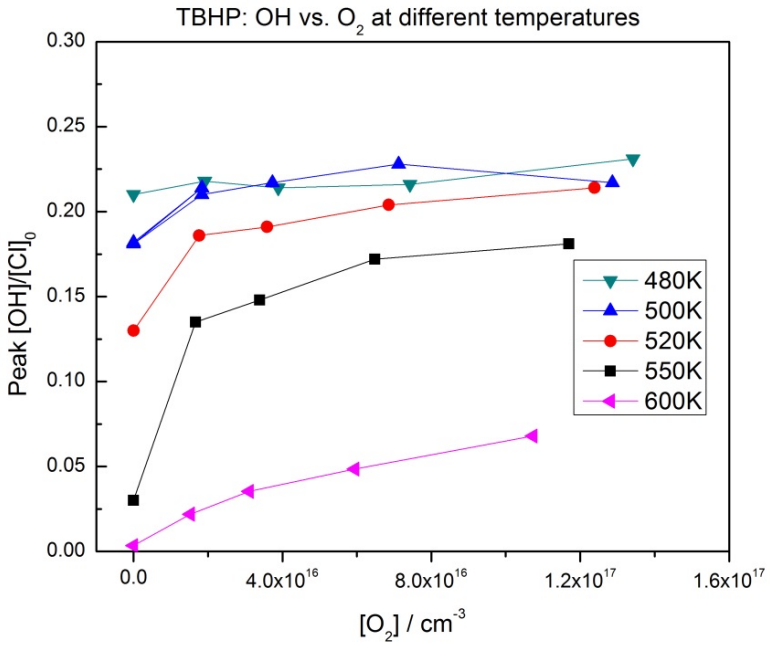

Figure 12. Peak OH yield vs. [O_2] between 480K and 600K in helium/TBHP/Cl_2/355nm system

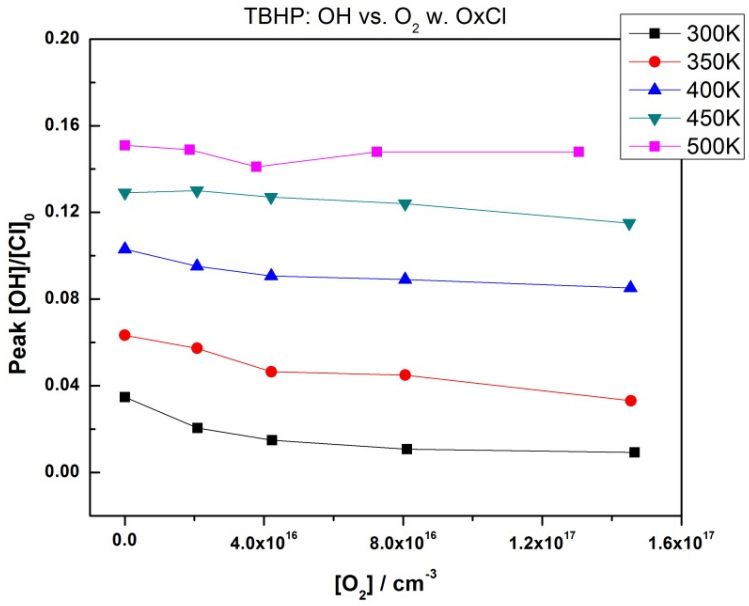

Figure 13. Peak OH yield vs. [O_2] between 300K and 500K in helium/TBHP/OxCl/355nm system

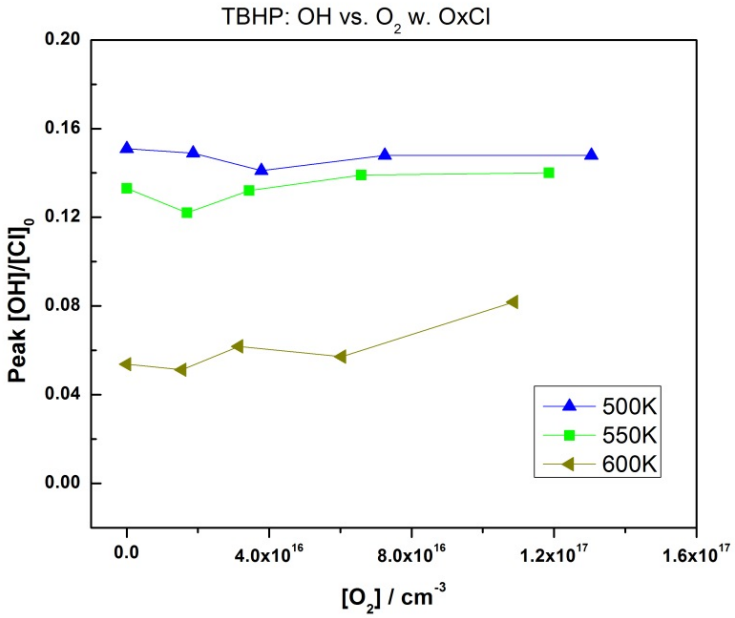

Figure 14. Peak OH yield vs. [O_2] between 500K and 600K in helium/TBHP/OxCl/355nm system

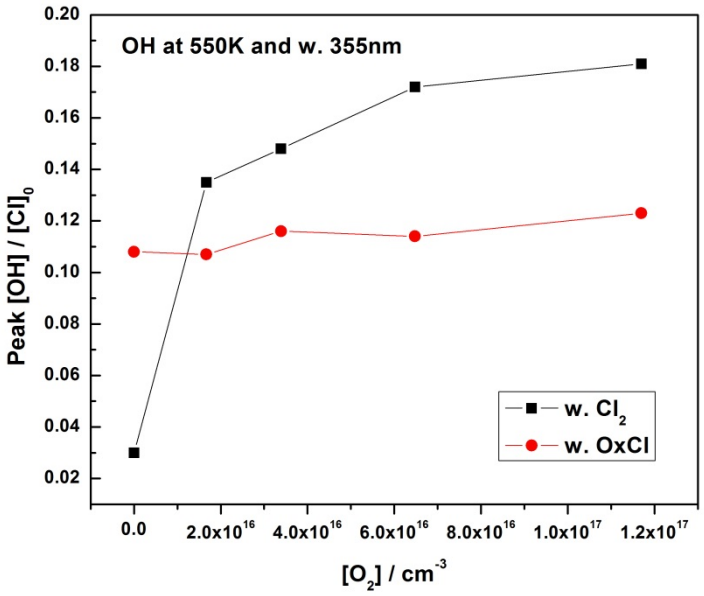

Figure 15. Peak OH yield vs. [O_2] at 550K in helium/TBHP/O_2/355nm with Cl_2 or OxCl as the Cl atom precursor

5. HO_2 Measurement

Figure 16 is a section of HO_2 $2\nu_1$ band [18]. The HO_2 absorption line we used is the one at 6625.784cm^{-1}. Unlike OH fundamental transitions, there is little data on the line intensities and pressure broadening coefficients of HO_2 transitions (both NIR and MIR). Fortunately, the methanol oxidation system has a near unity yield of HO_2 and CH_2O because of the reactions (R1) and (R2). Therefore, it is a perfect reference system for quantitative HO_2 or CH_2O measurement. The Excel worksheet for HO_2 measurement is in Appendix B and the data processing program is given in Appendix C. An effective absorption cross-section of HO_2 is introduced to calculate HO_2 concentrations (see Appendix B for the details).

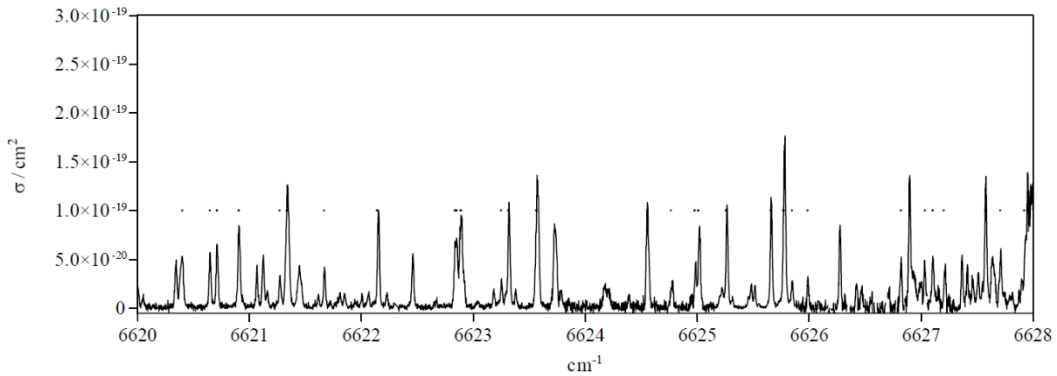

Figure 16. HO_2 lines of $2\nu_1$ band [18]

Figure 17 gives one example of this normalization. The red trace is of methanol system and has a peak HO_2 yield near time zero close to one. The black trace is the measured HO_2 in 1-butanol oxidation. Both measurements were run back-to-back under the same experimental conditions such as temperature, pressure, helium, oxygen and Cl precursor concentrations. After normalized to that of methanol system, the peak HO_2 yield near time zero in 1-butanol oxidation is measured to be about 40%.

Figure 18 is the HO_2 time profiles at different temperatures in 1-butanol oxidation measured by the above method.

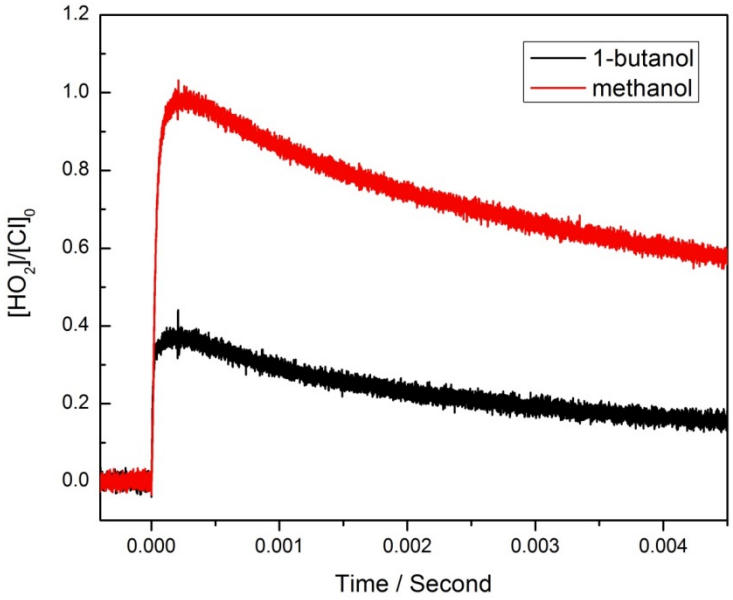

Figure 17. Measured HO_2 signal in 1-butanol oxidation is normalized to that of methanol oxidation reference system. Both traces are after background subtraction.

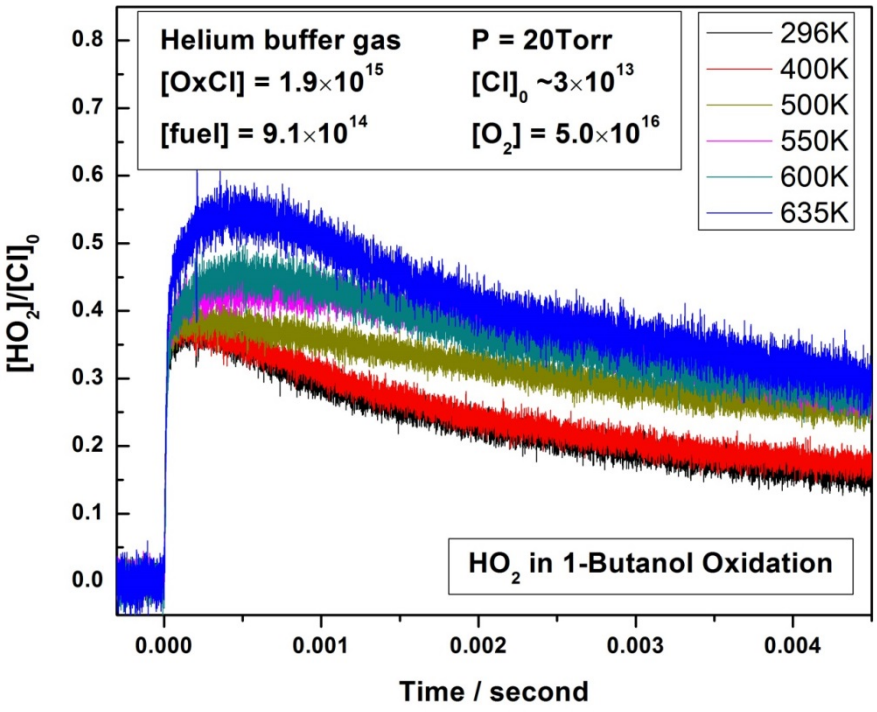

Figure 18. HO_2 yield time profiles at different temperatures in 1-butanol oxidation

6. CH_2O Measurement

Same as HO_2 measurement, the measured CH_2O signal in fuel oxidation reactions is normalized to that of methanol oxidation. CH_2O is probed near 3574nm. Methanol has weak absorption features in this region. We have carefully tried multiple wavelengths (e.g. 2814.7434cm^{-1}), and found 2797.9648cm^{-1} [14, 22] (2797.962cm^{-1} by the wavemeter WA-1500) is one of the optimum wavelengths (e.g. 2758.8062, 2761.4941, 2766.4150 and 2781.0347cm^{-1}) with least interference from methanol absorption. Figure 19 shows a section of the spectrum of CH stretch fundamental transitions of CH_2O, and Figure 20 is a simulated spectrum of CH_2O near 2797.9648cm^{-1} based on HITRAN database.

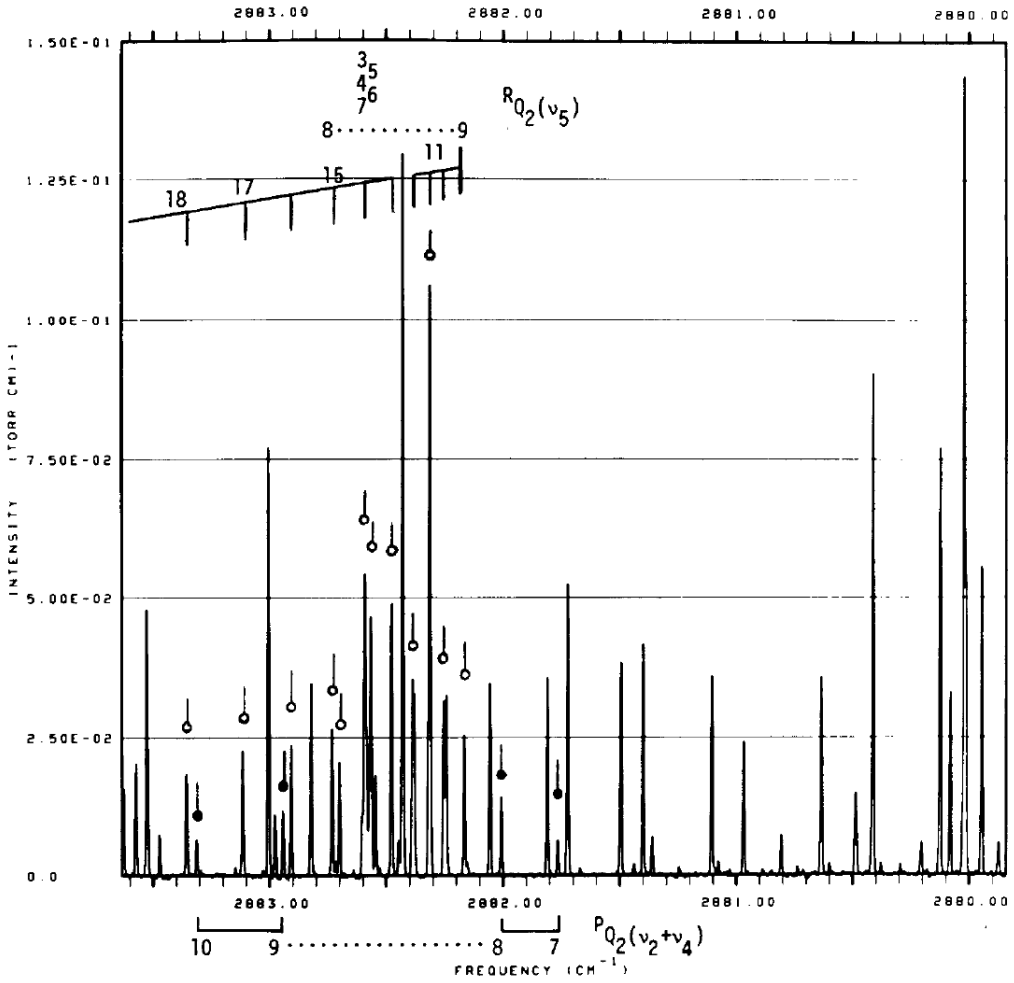

Figure 19. A section of the spectrum of CH stretch fundamental transitions of CH_2O [22]

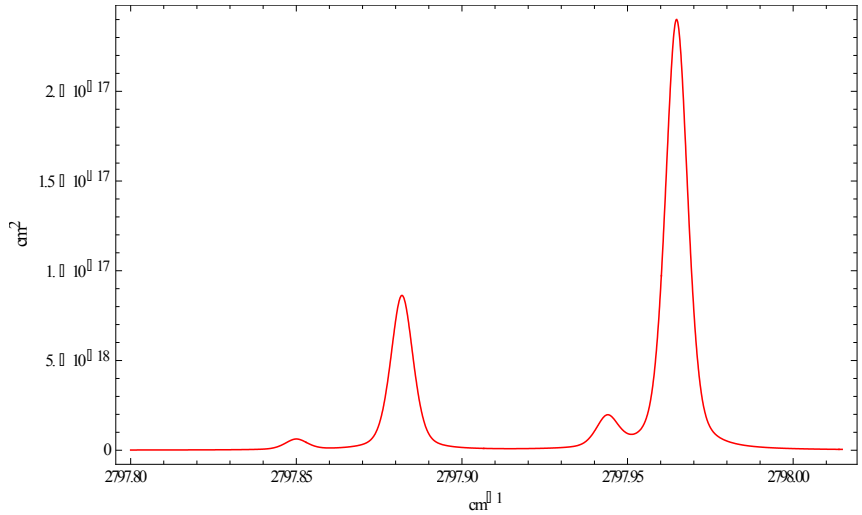

Figure 20. Simulated CH_2O spectrum near 2797.9648cm^{-1} at 20Torr air and 296K based on HITRAN database [14]

Figures 21 and 22 show the measured CH_2O concentrations at different temperatures in 1-butanol oxidation reactions, with and without oxygen respectively. Figure 21 (if $T \geq 500K$) and Figure 22 (if $T \geq 600K$) clearly show two time scales of CH_2O generation.

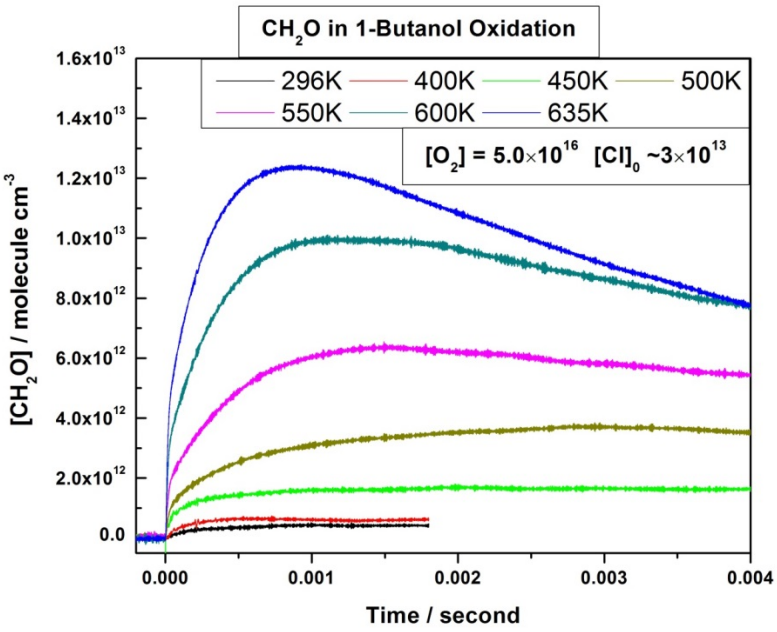

Figure 21. CH_2O generation in 1-butanol oxidation

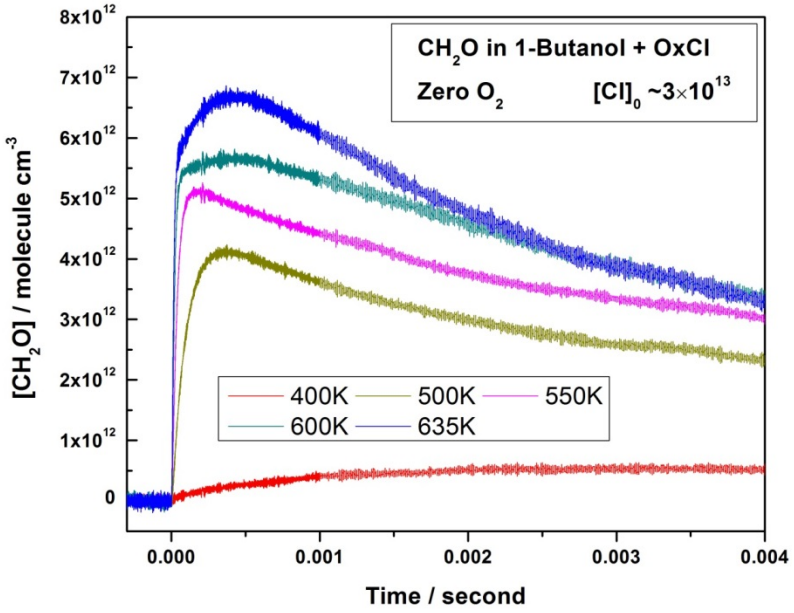

Figure 22. CH_2O generation in 1-butanol system with oxygen turned off

For 1-butanol and with the probe laser tuned to CH_2O absorption peak, we found lots of CH_2O will be generated even before photolysis laser pulses trigger the chemistry if the temperature is higher than 550K, Cl_2 is used as precursor and oxygen is turned off, as shown in Figure 23. The reason for this pre-trigger CH_2O generation is unknown to us. Adding O_2 will suppress CH_2O greatly but not completely. If OxCl is used, the probed CH_2O is much less when oxygen is turned off. Figure 23 clearly shows that OxCl is a better Cl precursor for 1-butanol oxidation study. Methanol system has the same problem as 1-butanol system if Cl_2 is the precursor (Figure 24). Interestingly, ethanol system does not show this problem (Figure 25).

We have measured CH_2O generation in the reaction $CH_2I + O_2$ [31, 32] by photolysis of CH_2I_2/O_2/helium mixture with either 355nm or 266nm laser. We found the yield of CH_2O is larger than 4 if 266nm laser is used and is only about 0.6 if 355nm laser is used. Both results are displayed in Figures 26 and 27 respectively. One possible explanation for this difference is 266nm laser has enough photon energy to dissociate CH_2I_2 molecule to generate CH_2 radical and I_2 molecule. [33] Figures 28 and 29 display the CH_2O generation near time zero of Figure 26 and 27. Both show two time scales of generation if oxygen concentration is higher than 1.3×10^{17}

molecule cm^{-3}. The fast generated CH_2O may correspond to the reaction channel $CH_2I + O_2 \rightarrow CH_2O + IO$, which only has a minor branching ratio with 355nm photolysis laser. [31, 32]

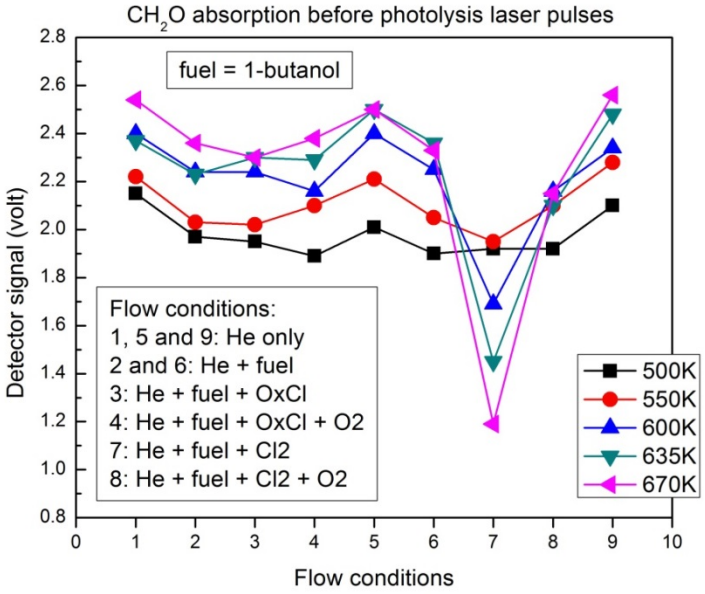

Figure 23. CH_2O generation before photolysis laser pulses under different conditions. Fuel molecule is 1-butanol.

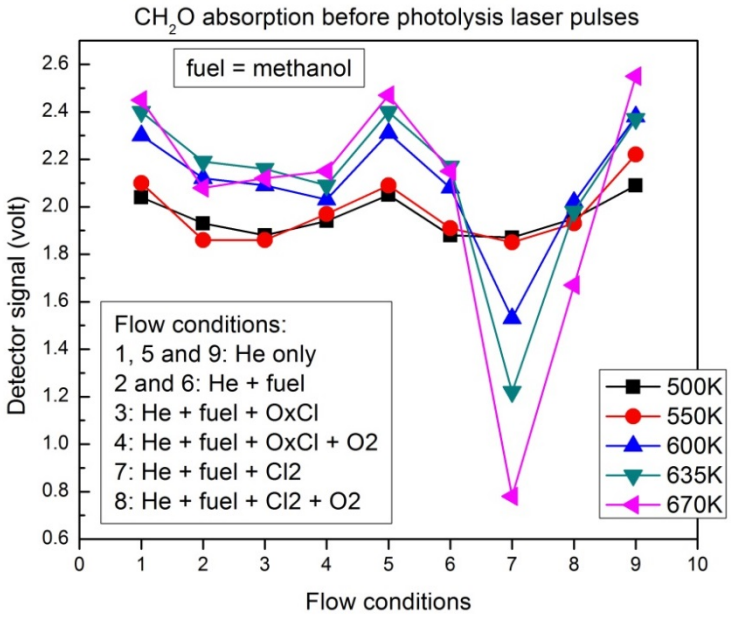

Figure 24. CH_2O generation before photolysis laser pulses under different conditions. Fuel molecule is methanol.

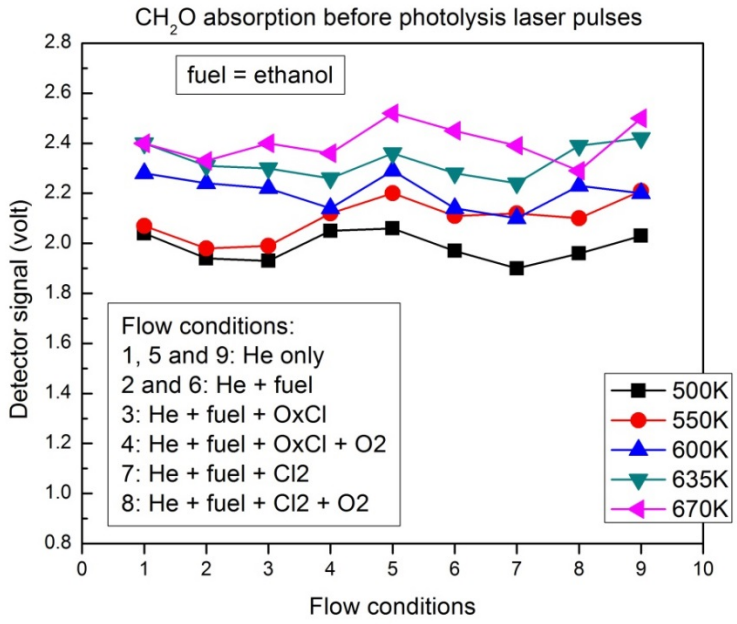

Figure 25. CH_2O generation before photolysis laser pulses under different conditions. Fuel molecule is ethanol.

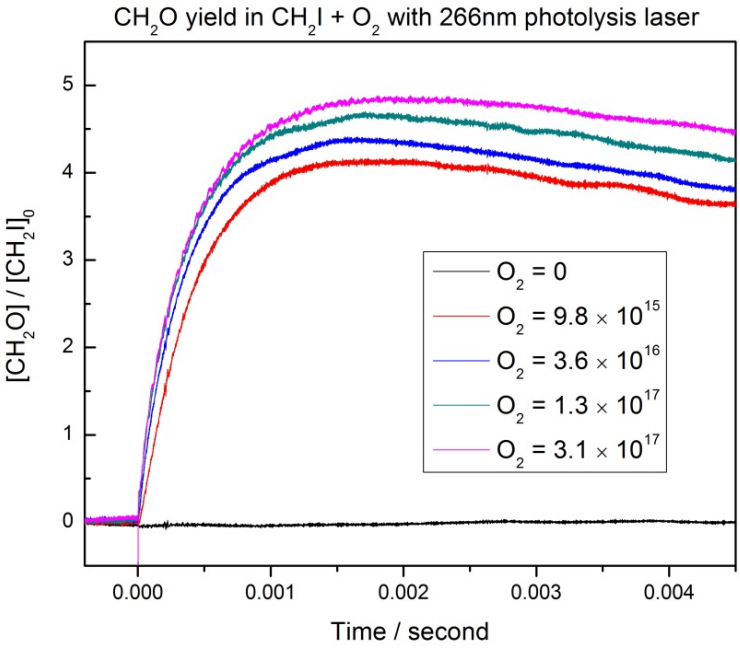

Figure 26. CH_2O yield vs. $[O_2]$ in $CH_2I + O_2$ with 266nm laser. The initial CH_2I concentration is 2.8×10^{12} molecule cm^{-3}.

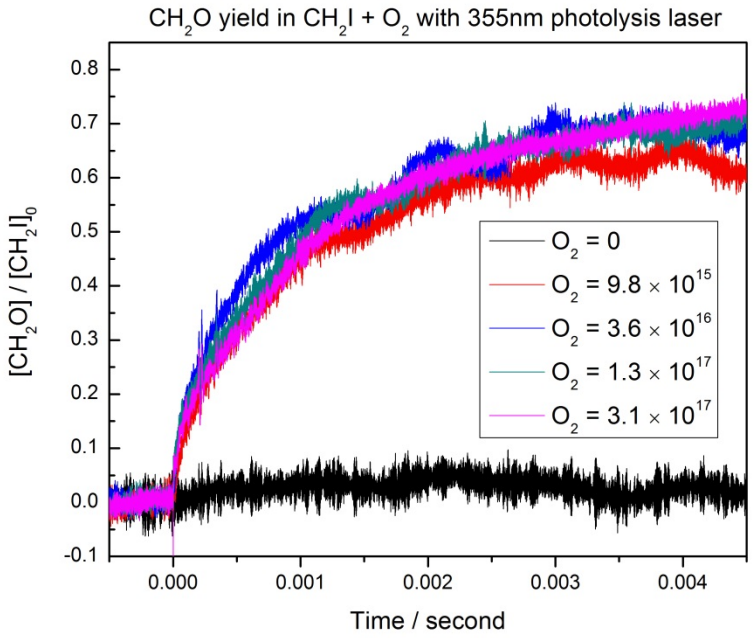

Figure 27. CH_2O yield vs. $[O_2]$ in $CH_2I + O_2$ with 355nm laser. The initial CH_2I concentration is 1.6×10^{12} molecule cm^{-3}.

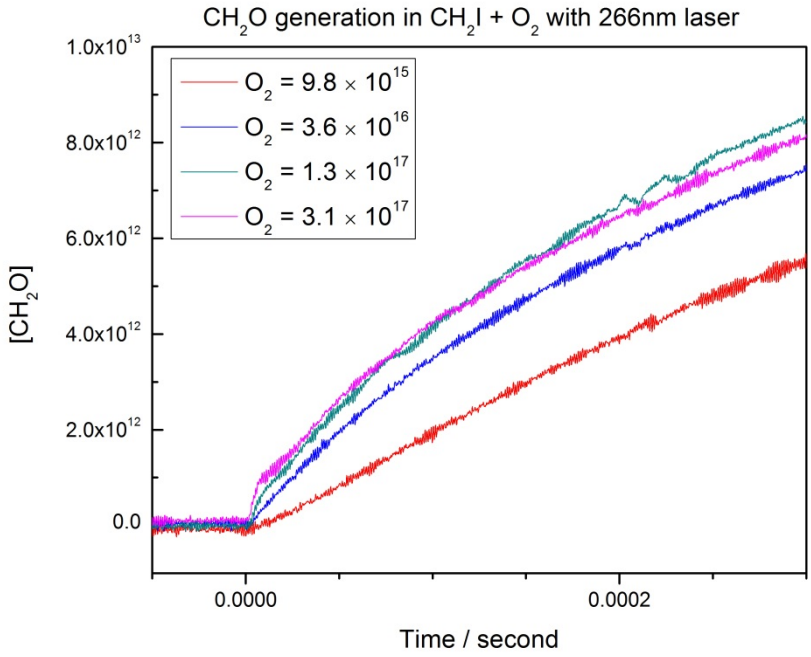

Figure 28. CH_2O generation near time zero in $CH_2I + O_2$ with 266nm laser. The initial CH_2I concentration is 2.8×10^{12} molecule cm^{-3}. The yield of fast generation CH_2O for the highest O_2 concentration is about 36%.

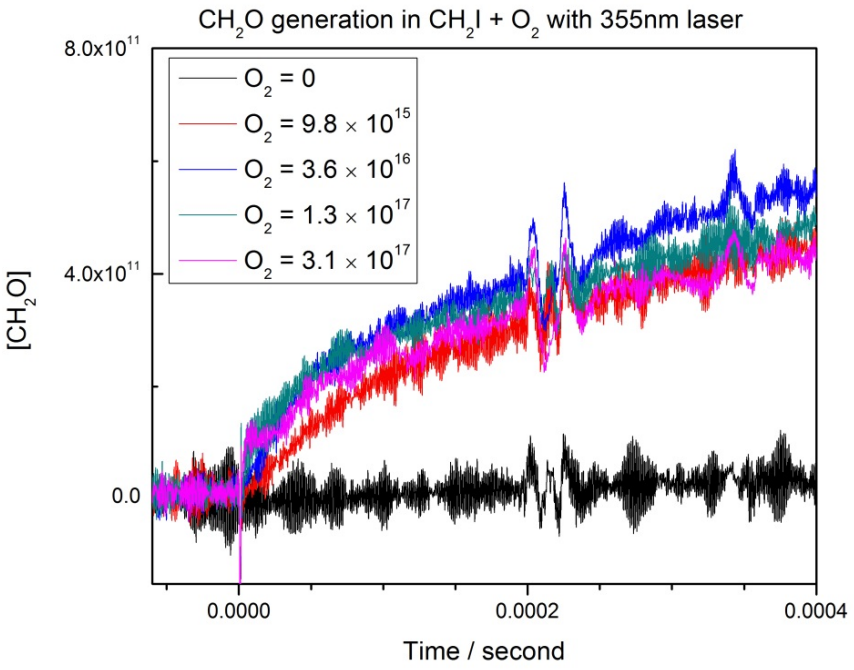

Figure 29. CH_2O generation near time zero in $CH_2I + O_2$ with 355nm laser. The initial CH_2I concentration is 1.6×10^{12} molecule cm^{-3}. The yield of fast generation CH_2O for the highest O_2 concentration is about several percent.

Appendix A

Gas correction factor calibrations for different MFCs. For each MFC, the first plot of each MFC is the measured gas factors and the fitted polynomial for the measured flow rate range; the second plot is the fractional error of the fitting. After the calibration, one should avoid the adjustments such as zero point or servo loop gain of the calibrated MFC.

MFC for fuel bubbler helium, full scale 2000sccm, **1.44 - 49.5 / x + 1.19E-5 x**

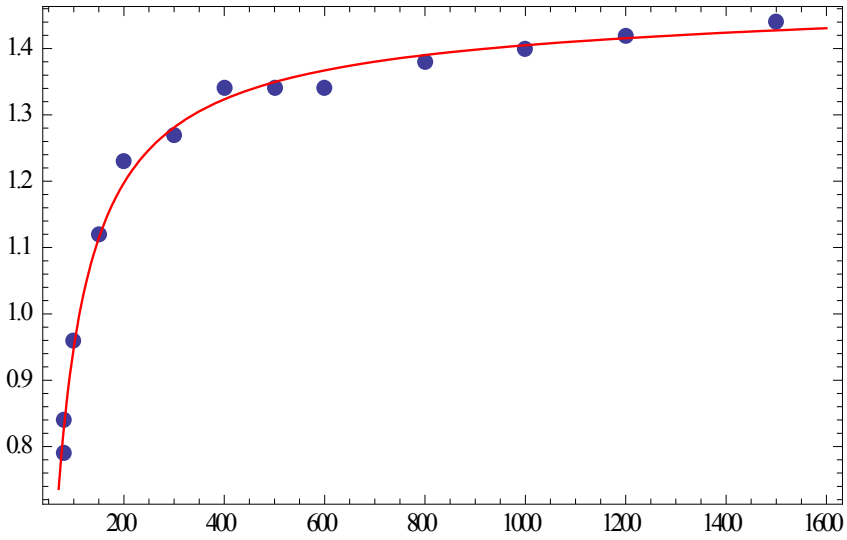

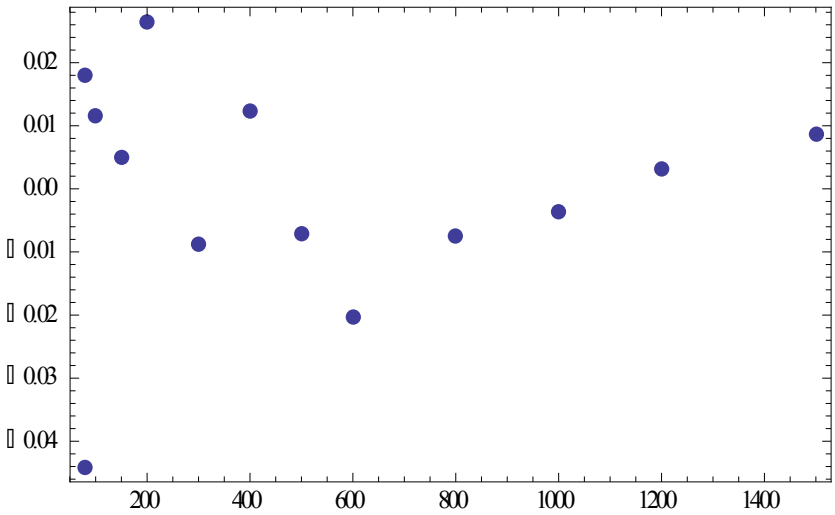

MFC for OxCl bubbler helium, full scale 20sccm, **1.24 + 9.58E-2 / x -1.84E-3 x**

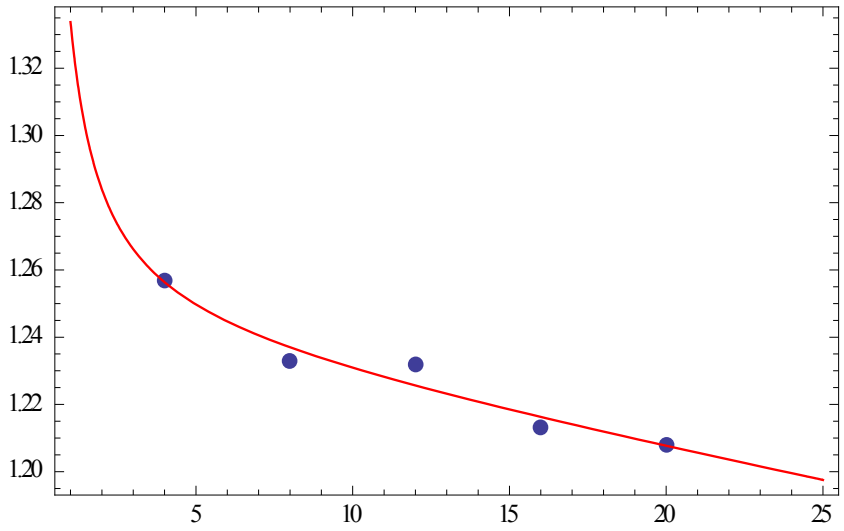

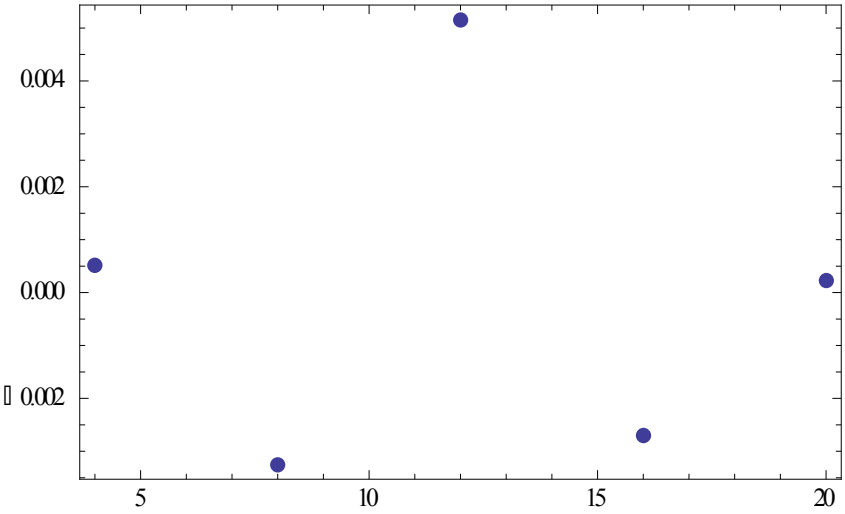

MFC for methanol bubbler helium, full scale 500sccm, **1.44 + 0.805 / x - 2.60E-4 x**

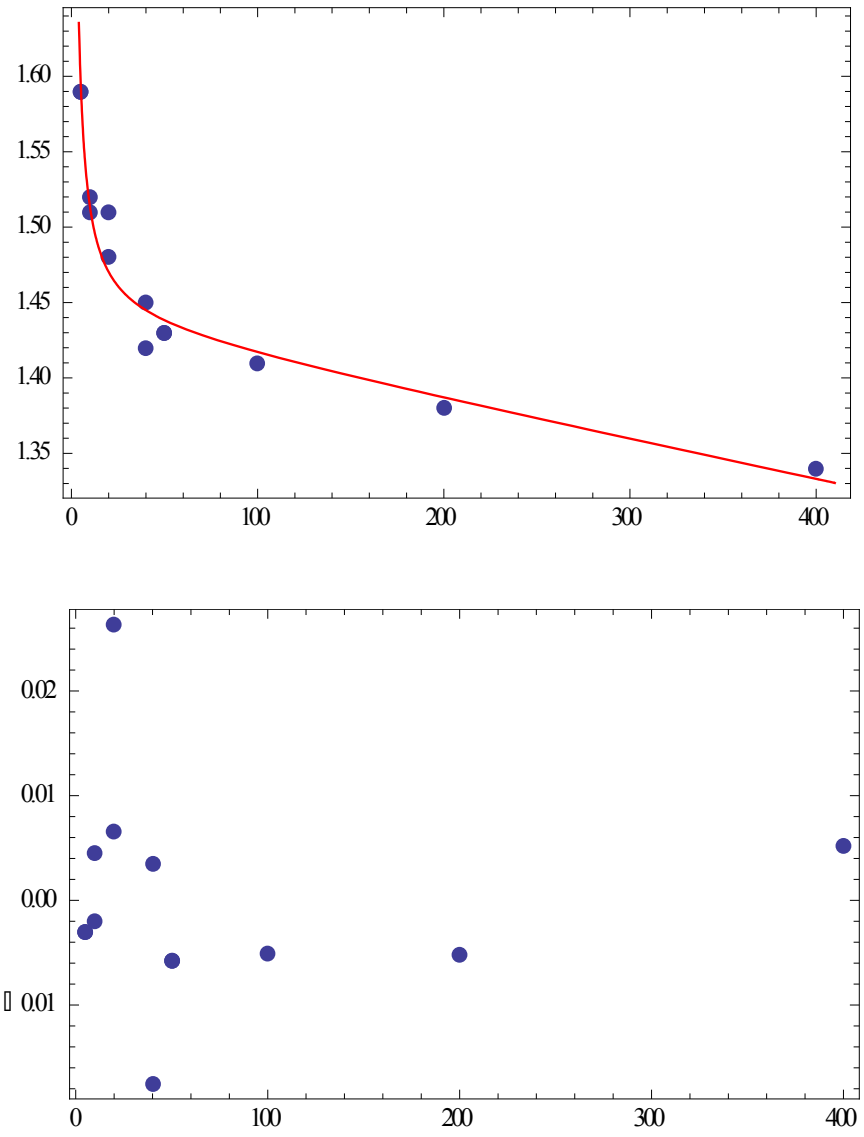

MFC for 5% Cl_2 in helium, full scale 100sccm, **1.40 + 5.42 / x - 1.19E-3 x**

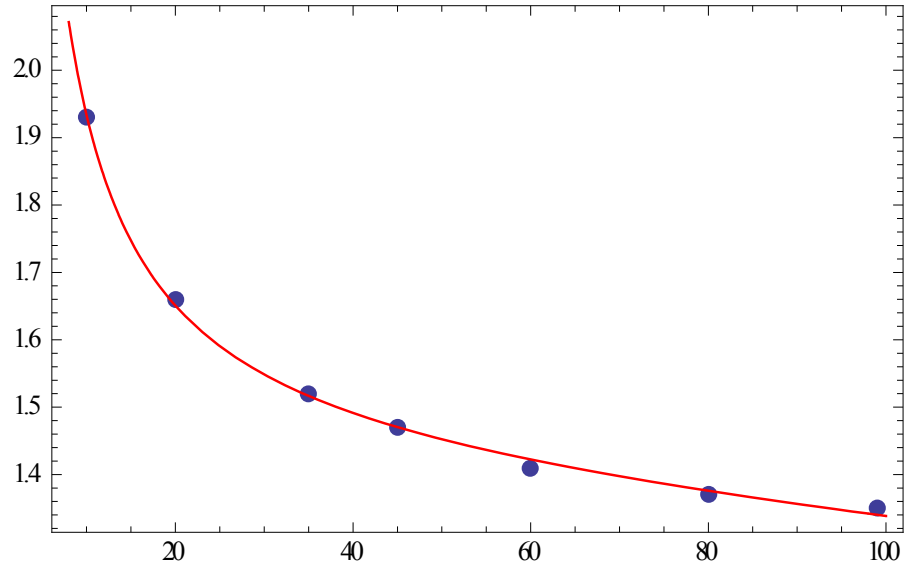

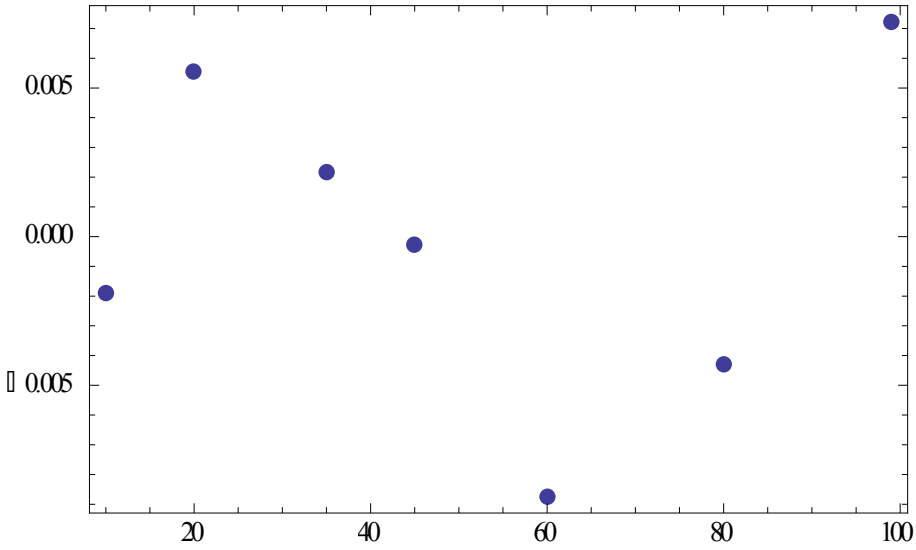

MFC for pure oxygen, full scale 1000sccm, **1.01 + 14.9 / x - 5.67E-5 x**

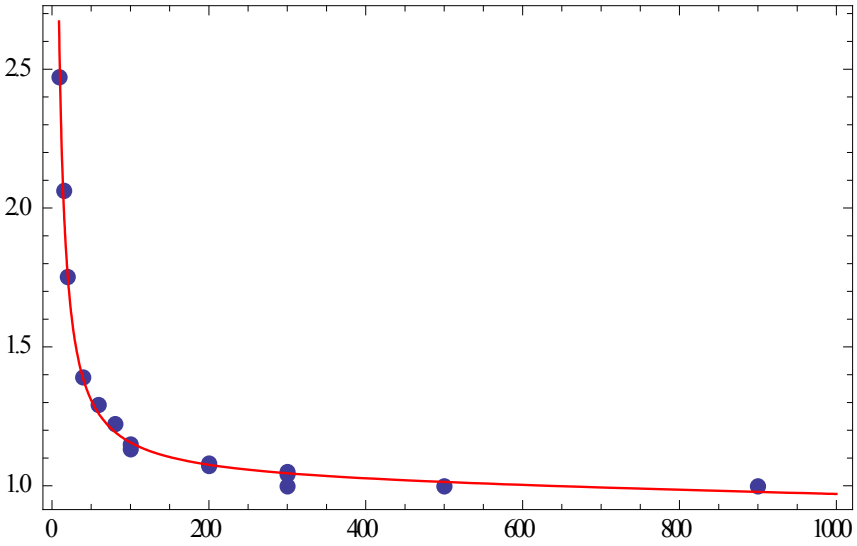

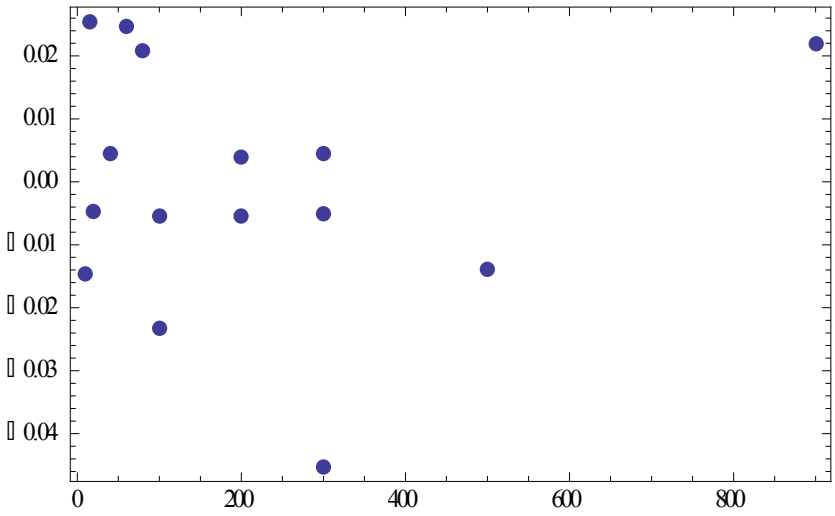

MFC for pure propane gas, full scale 50sccm, **0.352 – 0.321/x + 8.19E-5 x**

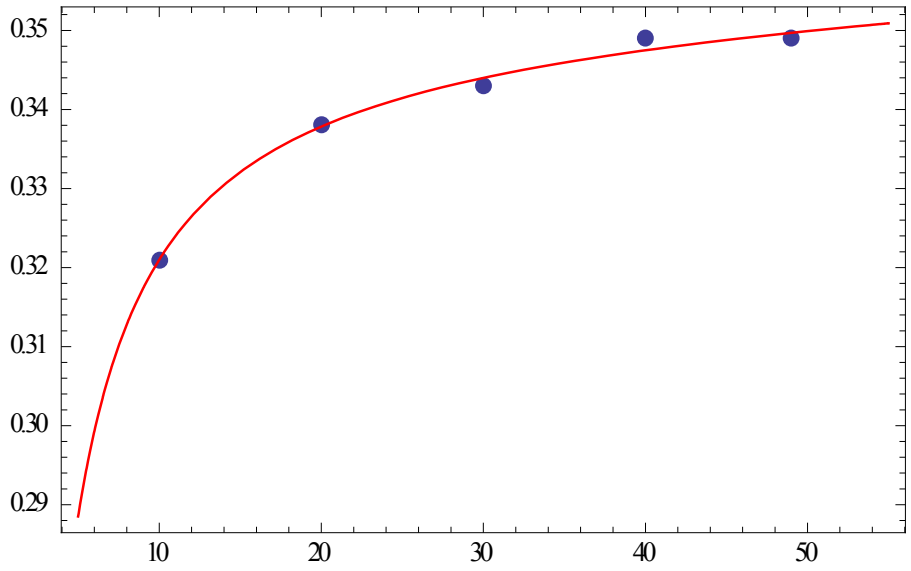

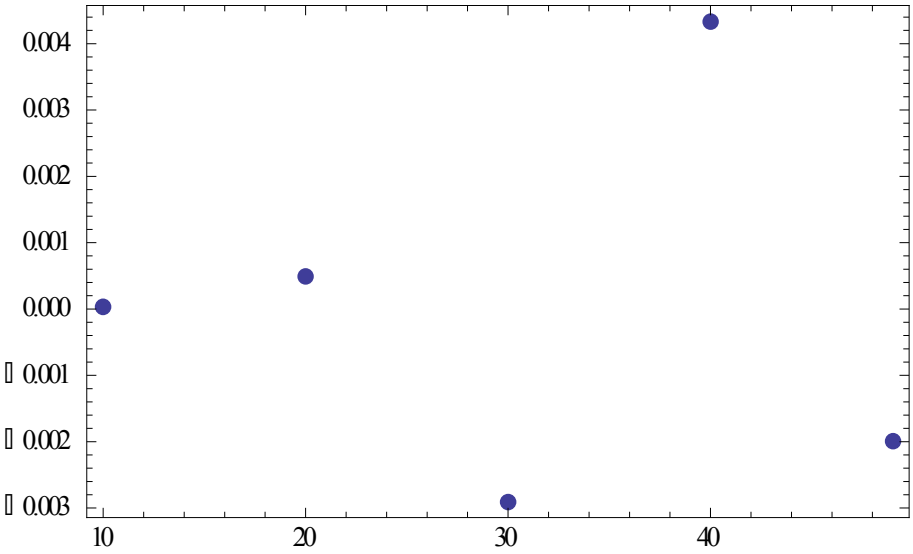

Appendix B

The Excel worksheet for HO_2 measurement has been divided into two parts: Figure 30-1 and Figure 30-2. Figure 30-1 is similar to Figure 7-1 for OH measurement and is mainly for designing flow conditions for experiments. The difference is the methanol oxidation is used as a reference system. In the measurement, HO_2 signal is compared with that in methanol oxidation under the "same" conditions, i.e. same temperature and pressure, same concentrations of helium, oxygen and Cl precursors. The exception is the fuel concentration, which may be different from methanol concentration. But because its concentration is relatively low, its effect to HO_2 absorption line is ignored. Another exception is when measuring HO_2 signal under zero-oxygen condition. For this case, a small amount of oxygen is added to the methanol oxidation system (row 23 in Figure 30-1).

Figure 30-2 is used to calculate the absolute HO_2 concentration of the studied fuel oxidation system by comparing the measured signal with that of methanol oxidation. One trick in the worksheet is something called "effective absorption cross section" in column AM. In methanol oxidation system, the initial Cl concentration is regarded to be equal to the peak HO_2 concentration. With the known absorption length, we can calculate the above cross section from the methanol HO_2 signal. This cross section is then used to calculate the HO_2 concentration in the fuel oxidation system studied. This effective absorption cross section can be different from the true value (but unknown) under the same conditions because of possible errors in absorption length determination and non-uniform distribution of HO_2 in the photolysis column.

It is straightforward to use this worksheet for CH_2O measurement, which uses the same reference system.

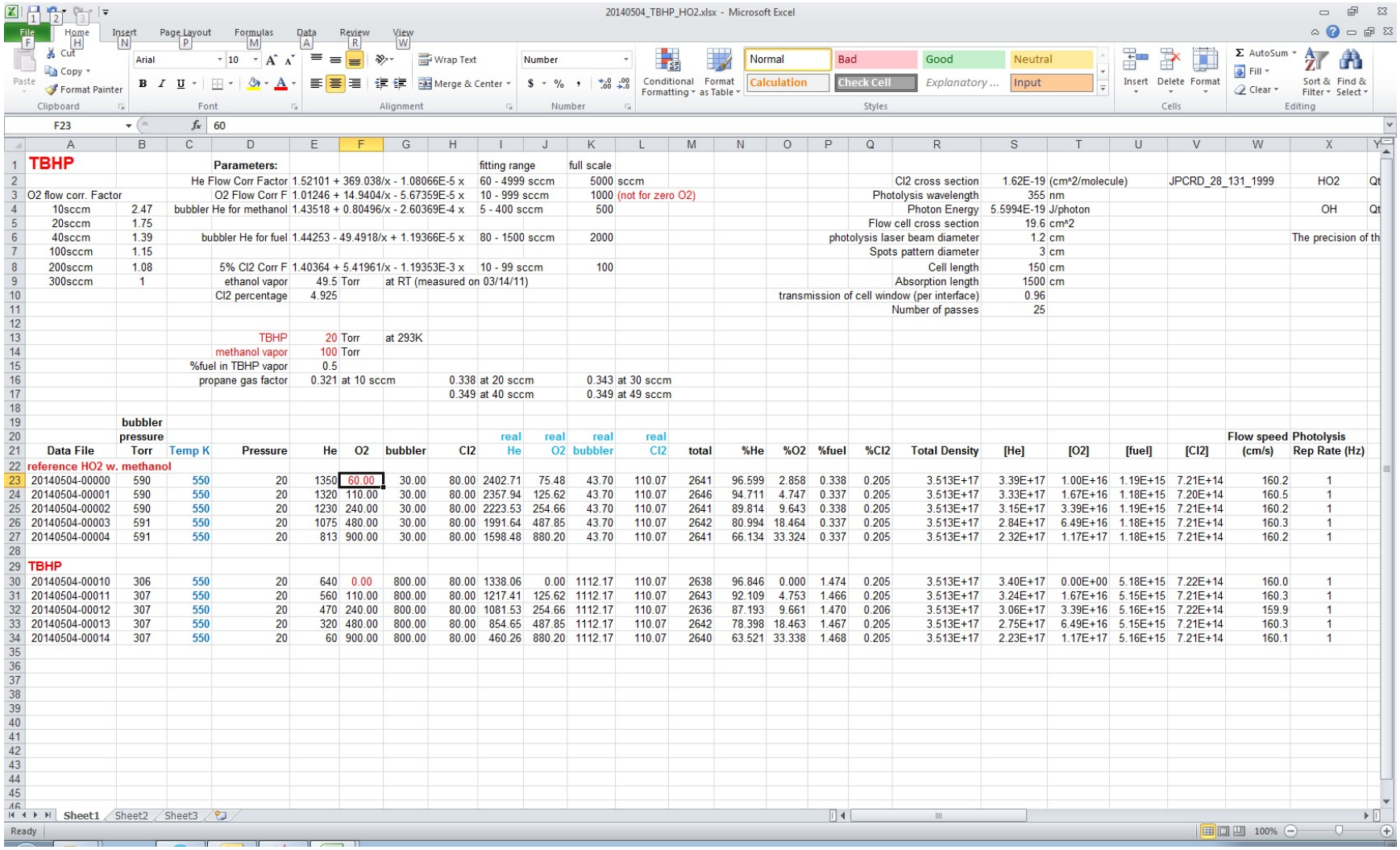

20140504_TBHP_HO2.xlsx - Microsoft Excel

	A	B	C	D	E	F	G	H	I	J	K	L	M	N	O	P	Q	R	S	T	U	V	W	X	Y
1	TBHP			Parameters:					fitting range		full scale														
2				He Flow Corr Factor	1.52101 + 369.038/x - 1.08066E-5 x				60 - 4999 sccm		5000	sccm						Cl2 cross section	1.62E-19	(cm^2/molecule)		JPCRD_28_131_1999		HO2	Qt
3	O2 flow corr. Factor			O2 Flow Corr F	1.01246 + 14.9404/x - 5.67359E-5 x				10 - 999 sccm		1000	(not for zero O2)						Photolysis wavelength	355	nm					
4	10sccm	2.47		bubbler He for methanol	1.43518 + 0.80496/x - 2.60369E-4 x				5 - 400 sccm		500							Photon Energy	5.5994E-19	J/photon				OH	Qt
5	20sccm	1.75																Flow cell cross section	19.6	cm^2					
6	40sccm	1.39		bubbler He for fuel	1.44253 - 49.4918/x + 1.19366E-5 x				80 - 1500 sccm		2000							photolysis laser beam diameter	1.2	cm				The precision of th	
7	100sccm	1.15																Spots pattern diameter	3	cm					
8	200sccm	1.08		5% Cl2 Corr F	1.40364 + 5.41961/x - 1.19353E-3 x				10 - 99 sccm		100							Cell length	150	cm					
9	300sccm	1		ethanol vapor	49.5	Torr	at RT (measured on 03/14/11)											Absorption length	1500	cm					
10				Cl2 percentage	4.925										transmission of cell window (per interface)				0.96						
11																		Number of passes	25						
12																									
13				TBHP	20	Torr	at 293K																		
14				methanol vapor	100	Torr																			
15				%fuel in TBHP vapor	0.5																				
16				propane gas factor	0.321	at 10 sccm		0.338	at 20 sccm		0.343	at 30 sccm													
17								0.349	at 40 sccm		0.349	at 49 sccm													
18																									
19		bubbler																							
20		pressure							real	real	real	real											Flow speed	Photolysis	
21	Data File	Torr	Temp K	Pressure	He	O2	bubbler	Cl2	He	O2	bubbler	Cl2	total	%He	%O2	%fuel	%Cl2	Total Density	[He]	[O2]	[fuel]	[Cl2]	(cm/s)	Rep Rate (Hz)	
22	reference HO2 w. methanol																								
23	20140504-00000	590	550	20	1350	60.00	30.00	80.00	2402.71	75.48	43.70	110.07	2641	96.599	2.858	0.338	0.205	3.513E+17	3.39E+17	1.00E+16	1.19E+15	7.21E+14	160.2	1	
24	20140504-00001	590	550	20	1320	110.00	30.00	80.00	2357.94	125.62	43.70	110.07	2646	94.711	4.747	0.337	0.205	3.513E+17	3.33E+17	1.67E+16	1.18E+15	7.20E+14	160.5	1	
25	20140504-00002	590	550	20	1230	240.00	30.00	80.00	2223.53	254.66	43.70	110.07	2641	89.814	9.643	0.338	0.205	3.513E+17	3.15E+17	3.39E+16	1.19E+15	7.21E+14	160.2	1	
26	20140504-00003	591	550	20	1075	480.00	30.00	80.00	1991.64	487.85	43.70	110.07	2642	80.994	18.464	0.337	0.205	3.513E+17	2.84E+17	6.49E+16	1.18E+15	7.21E+14	160.3	1	
27	20140504-00004	591	550	20	813	900.00	30.00	80.00	1598.48	880.20	43.70	110.07	2641	66.134	33.324	0.337	0.205	3.513E+17	2.32E+17	1.17E+17	1.18E+15	7.21E+14	160.2	1	
28																									
29	TBHP																								
30	20140504-00010	306	550	20	640	0.00	800.00	80.00	1338.06	0.00	1112.17	110.07	2638	96.846	0.000	1.474	0.205	3.513E+17	3.40E+17	0.00E+00	5.18E+15	7.22E+14	160.0	1	
31	20140504-00011	307	550	20	560	110.00	800.00	80.00	1217.41	125.62	1112.17	110.07	2643	92.109	4.753	1.466	0.205	3.513E+17	3.24E+17	1.67E+16	5.15E+15	7.21E+14	160.3	1	
32	20140504-00012	307	550	20	470	240.00	800.00	80.00	1081.53	254.66	1112.17	110.07	2636	87.193	9.661	1.470	0.206	3.513E+17	3.06E+17	3.39E+16	5.16E+15	7.22E+14	159.9	1	
33	20140504-00013	307	550	20	320	480.00	800.00	80.00	854.65	487.85	1112.17	110.07	2642	78.398	18.463	1.467	0.205	3.513E+17	2.75E+17	6.49E+16	5.15E+15	7.21E+14	160.3	1	
34	20140504-00014	307	550	20	60	900.00	800.00	80.00	460.26	880.20	1112.17	110.07	2640	63.521	33.338	1.468	0.205	3.513E+17	2.23E+17	1.17E+17	5.16E+15	7.21E+14	160.1	1	

Figure 30-1. Excel worksheet for HO_2 measurement

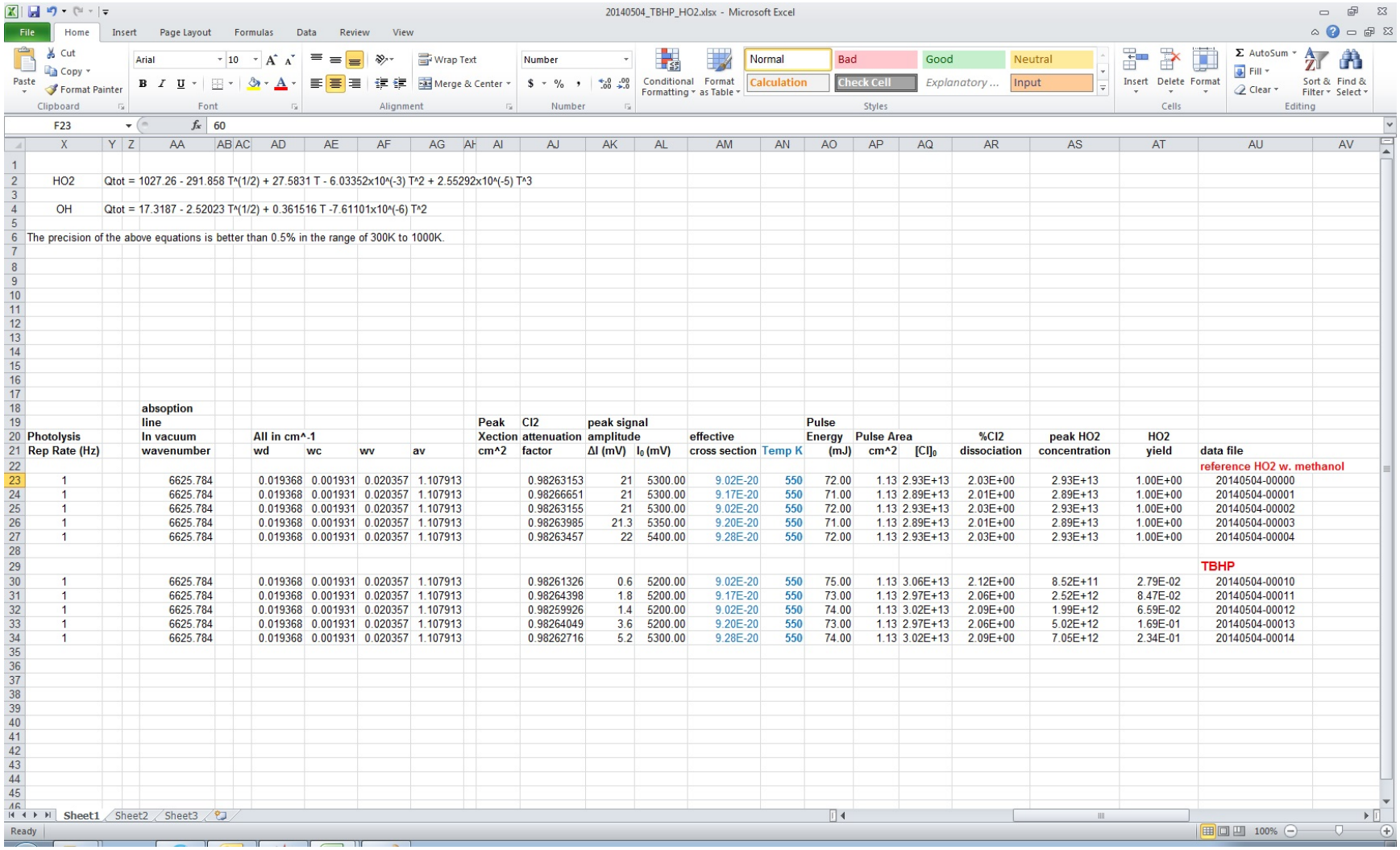

Figure 30-2. Excel worksheet for HO_2 measurement. Effective absorption cross-section is used to calculate HO_2 concentrations.

Appendix C

Data processing program in Mathematica for OH measurement with notes written in-between asterisks, e.g. (*…*)

Calculate OH concentration in Cl-initiated fuel oxidation experiments probed by cw OPO laser

```
Tp = 300; cl0 = 4.32 × 10^13;(* temperature and initial Cl concentration *)

address = "D:\\CRF_Data_2\\2014-06-10\\";(* file path *)
file = "20140610-00000"; I0 = 10.8;(* name of the on-peak data file and its I_0 *)
data0 = Import[address <> "F1" <> file <> ".csv", "CSV"];
(* import data file, which is always in CSV format. "F1"
 because F1 averaging math channel saved by the oscilloscope  *)
n0 = Length[data0]; (* length of data0 *)
data1 = Take[data0, {6, n0}];
(* the first 5 elements of data0 are of the settings of oscilloscope *)
n1 = Length[data1](* length of data1 *)
```

```
50 001
```

```
address2 = address;
file2 = "20140610-00004"; I00 = 10.8;(* name of the off-peak data file and its I_0 *)
data02 = Import[address2 <> "F1" <> file2 <> ".csv", "CSV"];
n02 = Length[data02];
data2 = Take[data02, {6, n02}];
n2 = Length[data2](* length of data2, make sure it is the same as n1 *)
t0 = data1[[1, 1]] 10^6;(* time of the first data point in microsecond *)
dt = 10^6 data1[[2, 1]] - t0;(* time step of data recording in microsecond *)
```

```
50 001
```

```
m = IntegerPart[n1 / 10] - 500;
(* the number of pre-photolysis data points used for offset adjustment *)
data3 = Table[data1[[i, 2]], {i, n1}];(* on-peak data trace ignoring time *)
os3 = (Sum[data3[[i]], {i, 1, m}]) / m;(* calculate the offset *)
data3 = (data3 - os3);(* offset adjustment,
now data3 is almost zero before photolysis *)
data4 = Table[data2[[i, 2]], {i, n1}];(* off-peak data trace ignoring time *)
os4 = (Sum[data4[[i]], {i, 1, m}]) / m;(* calculate the offset *)
data4 = (data4 - os4);(* offset adjustment,
now data4 is almost zero before photolysis *)
data5 = data3 - (I0 / I00) data4;(* on-peak trace subtracted by off-
 peak trace to remove commnon mode noise (scaled to both I_0) *)
os5 = (Sum[data5[[i]], {i, 1, m}]) / m;(* calculate the offset *)
data5 = data5 - os5;(* offset adjustment,
now data5 is almost zero before photolysis *)
```

```
ni = 4000; nf = 25 000;
(* this paragraph is to check how good the background subtraction is. The off-
 peak trace can have small depletion or absorption. Normally multiple off-
 peak traces near the OH absorption peak are measured to check if
  the small depletion or absorption is uniform near the peak. *)
vmax = 0.2; vmin = -0.03; (* plot range of the signal *)
fig1 = ListPlot[Take[data3, {ni, nf}], Frame → True,
  PlotRange → {{0, nf - ni}, {vmin, vmax}}, Axes → False, Joined → True]
  (* plot the on-peak raw data *)
fig2 = ListPlot[Take[data4, {ni, nf}], Frame → True,
  PlotRange → {{0, nf - ni}, {vmin, vmax}}, Axes → False, Joined → True]
  (* plot the off-peak raw data *)
fig3 = ListPlot[Take[data5, {ni, nf}], Frame → True,
  PlotRange → {{0, nf - ni}, {vmin, vmax}}, Axes → False, Joined → True]
  (* data trace after background subtraction,
 peak voltage is used to calculate peak OH yield in the Excel worksheet *)
```

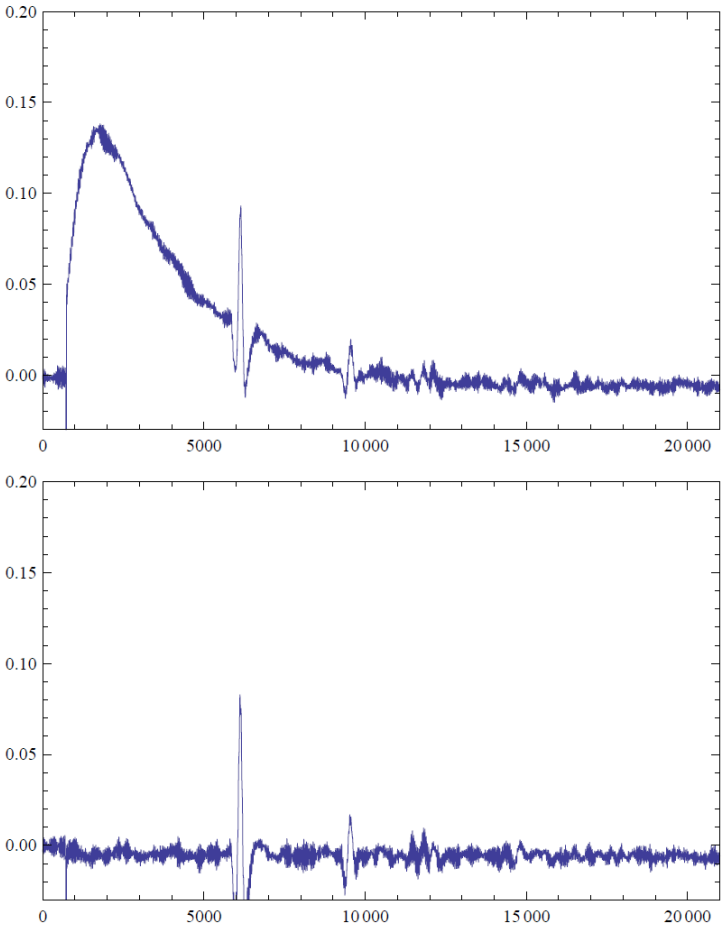

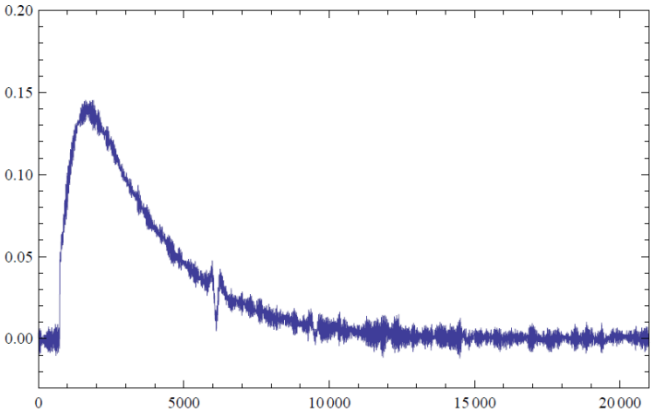


```
σ = 4.64 × 10^-18;
(* OH peak absorption cross section calculated by the Excel worksheet *)
abl = 1625;(* absorption length calculated by the Excel worksheet *)
concentration = Log[I0 / (I0 - data5)] / (abl * σ);
(* calculate concentration time profile *)
ListPlot[concentration, Frame → True, PlotRange → All,
 Axes → False, Joined → True, FrameLabel → {"Data Point", "molecule/cm^3"}]
 (* plot the whole concentration profile *)
```

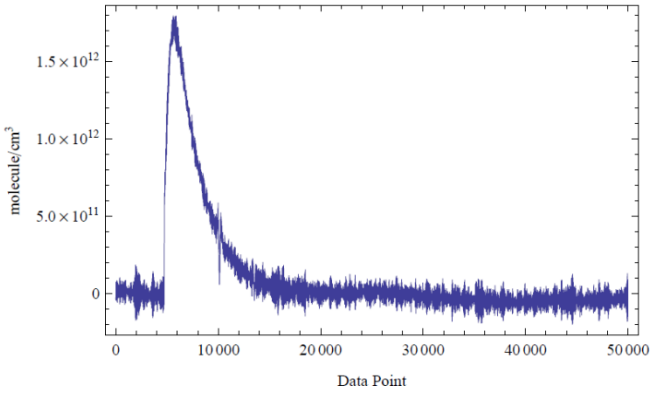


```
ListPlot[Take[concentration, {ni, nf}], Frame → True,
 PlotRange → All, Axes → False, Joined → True](* zoom in a little bit *)
```

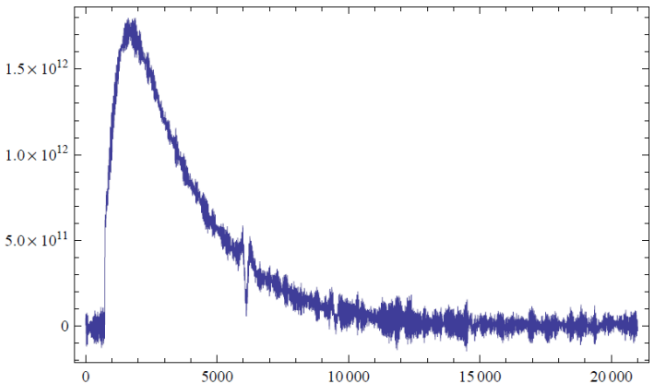

```
result = Table[{0, 0}, {i, 1, n1 + 2}];
(* this paragraph exports the calculated OH time proile,
normalized to the initial Cl concentration *)
result[[1]] = {"time", "OH"};
result[[2]] = {"us", ToString[Tp] <> "K"};
(* time is in micro second, and temperature *)
For[i = 3, i < n1 + 3, i++, result[[i]] =
  {SetPrecision[t0 + dt * (i - 3), 5], SetPrecision[concentration[[i - 2]] / cl0, 4]}];
(* time is generated with t0 and dt *)
Export[address <> file <> ".txt", result, "TSV"]
(* export the results to the same directory *)
Mean[Take[concentration, 500]]
(* average of the first 500 concentrtion data points *)
StandardDeviation[Take[concentration, 500]]
(* standard error of the first 500 concentrtion data points,
used as an estimation of the detection limit of the experiments *)
```

```
D:\CRF_Data_2\2014-06-10\20140610-00000.txt
```

$$1.53098 \times 10^{10}$$

$$3.84262 \times 10^{10}$$

Data processing program in Mathematica for HO_2 measurement with notes written in-between asterisks, e.g. (*…*)

Calculate HO2 concentration in Cl-initiated fuel oxidation experiments probed by NIR diode laser

```
Tp = 550; cl0 = 2.93 × 10^13;(* temperature and initial Cl concentration *)

address = "D:\\CRF_Data\\2014-05-04\\";(* file path *)
file = "20140504-00000"; I0 = 5.3;(* name of the on-peak data file and its I_0 *)
data0 = Import[address <> "F1" <> file <> ".csv", "CSV"];
(* import data file, which is always in CSV format. "F1"
 because F1 averaging math channel saved by the oscilloscope  *)
n0 = Length[data0]; (* length of data0 *)
data1 = Take[data0, {6, n0}];
(* the first 5 elements of data0 are of the settings of oscilloscope *)
n1 = Length[data1](* length of data1 *)
```

125 001

```
address2 = address;
file2 = "20140504-00009"; I00 = 5.15;(* name of the off-peak data file and its I_0 *)
data02 = Import[address2 <> "F1" <> file2 <> ".csv", "CSV"];
n02 = Length[data02];
data2 = Take[data02, {6, n02}];
n2 = Length[data2](* length of data2, make sure it is the same as n1 *)
t0 = data1[[1, 1]] 10^6;(* time of the first data point in microsecond *)
dt = 10^6 data1[[2, 1]] - t0;(* time step of data recording in microsecond *)
```

125 001

```
m = IntegerPart[n1 / 10] - 500;
(* the number of pre-photolysis data points used for offset adjustment *)
data3 = Table[data1[[i, 2]], {i, n1}];(* on-peak data trace ignoring time *)
os3 = (Sum[data3[[i]], {i, 1, m}]) / m;(* calculate the offset *)
data3 = (data3 - os3);(* offset adjustment,
now data3 is almost zero before photolysis *)
data4 = Table[data2[[i, 2]], {i, n1}];(* off-peak data trace ignoring time *)
os4 = (Sum[data4[[i]], {i, 1, m}]) / m;(* calculate the offset *)
data4 = (data4 - os4);(* offset adjustment,
now data4 is almost zero before photolysis *)
data5 = data3 - (I0 / I00) data4;(* on-peak trace subtracted by off-
 peak trace to remove commnon mode noise (scaled to both I_0) *)
os5 = (Sum[data5[[i]], {i, 1, m}]) / m;(* calculate the offset *)
data5 = data5 - os5;(* offset adjustment,
now data5 is almost zero before photolysis *)
```

```
ni = 6000; nf = 50 000;
(* this paragraph is to check how good the background subtraction is. The off-
 peak trace can have small depletion or absorption. Normally multiple off-
 peak traces near the HO2 absorption peak are measured to check
  if the small depletion or absorption is uniform near the peak. *)
vmax = 0.03; vmin = -0.02;(* plot range of the signal *)
fig1 = ListPlot[Take[data3, {ni, nf}], Frame → True,
  PlotRange → {{0, nf - ni}, {vmin, vmax}}, Axes → False, Joined → True]
  (* plot the on-peak raw data *)
fig2 = ListPlot[Take[data4, {ni, nf}], Frame → True,
  PlotRange → {{0, nf - ni}, {vmin, vmax}}, Axes → False, Joined → True]
  (* plot the off-peak raw data *)
fig3 = ListPlot[Take[data5, {ni, nf}], Frame → True,
  PlotRange → {{0, nf - ni}, {vmin, vmax}}, Axes → False, Joined → True]
  (* data trace after background subtraction,
 peak voltage is used to calculate peak HO2 yield in the Excel worksheet *)
```

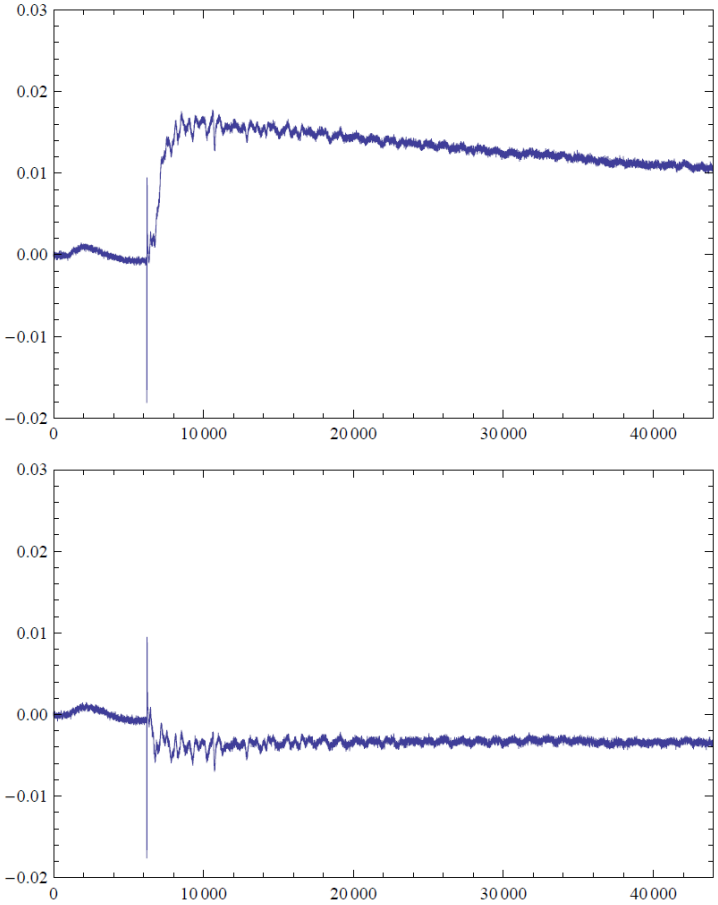

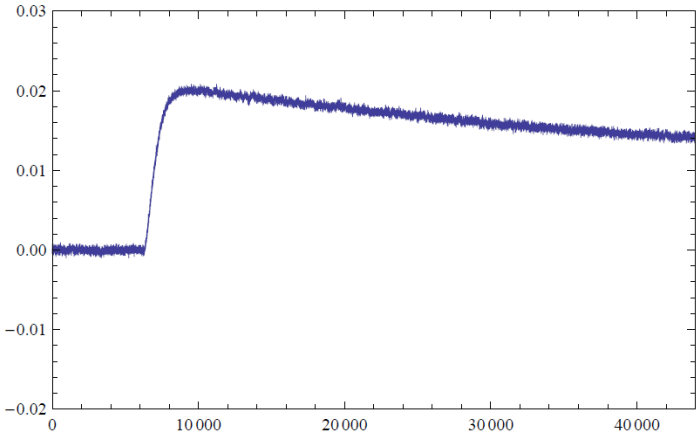


```
σ = 9.02 × 10^-20;(* effective HO2 peak absorption cross section
 calculated by the Excel worksheet. Measured HO2 signal is normalized
 to that of methanol system, which has a near unity HO2 yield. *)
abl = 1500;(* absorption length calculated by the Excel worksheet *)
concentration = Log[I0 / (I0 - data5)] / (abl * σ);
(* calculate concentration time profile *)
ListPlot[concentration, Frame → True, PlotRange → All,
 Axes → False, Joined → True, FrameLabel → {"Data Point", "molecule/cm^3"}]
 (* plot the whole concentration profile *)
```

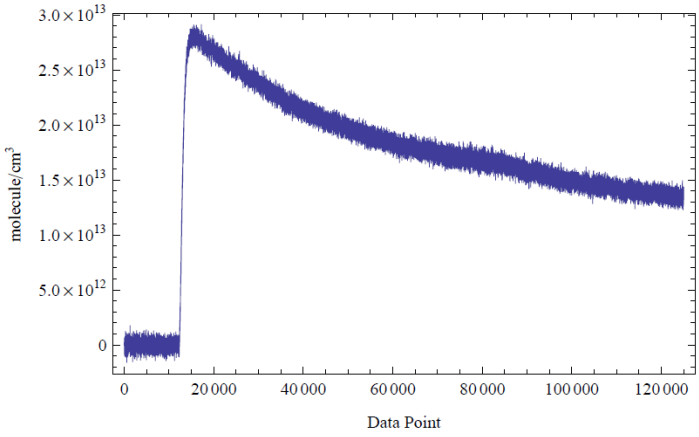

```
ListPlot[Take[concentration, {ni, nf}], Frame → True,
 PlotRange → All, Axes → False, Joined → True](* zoom in a little bit *)
```

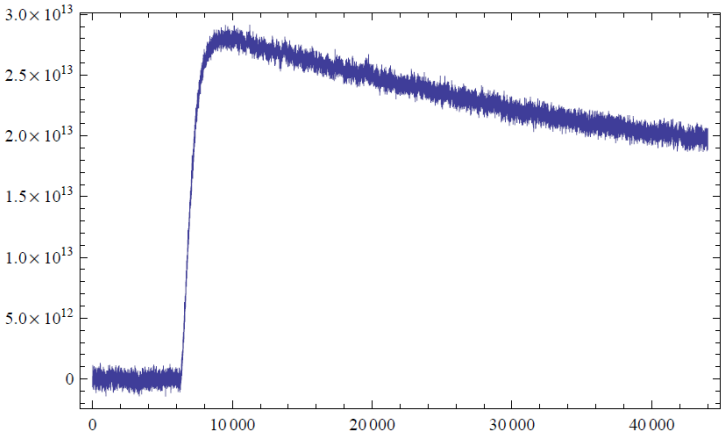


```
result = Table[{0, 0}, {i, 1, n1 + 2}];
(* this paragraph exports the calculated HO2 time proile,
normalized to the initial Cl concentration *)
result[[1]] = {"time", "HO2"};
result[[2]] = {"us", ToString[Tp] <> "K"};
(* time is in micro second, and temperature *)
For[i = 3, i < n1 + 3, i++, result[[i]] =
  {SetPrecision[t0 + dt * (i - 3), 5], SetPrecision[concentration[[i - 2]] / c10, 4]}];
(* time is generated with t0 and dt *)
Export[address <> file <> ".txt", result, "TSV"]
(* export the results to the same directory *)
Mean[Take[concentration, 500]]
(* average of the first 500 concentrtion data points *)
StandardDeviation[Take[concentration, 500]]
(* standard error of the first 500 concentrtion data points,
used as an estimation of the detection limit of the experiments *)
```

```
C:\Haifeng\CRF_Data\2014-05-04\20140504-00000.txt
```

$$1.75627 \times 10^{10}$$

$$3.78552 \times 10^{11}$$

References

1. Battin-Leclerc, F., *Detailed chemical kinetic models for the low-temperature combustion of hydrocarbons with application to gasoline and diesel fuel surrogates.* Prog. Energy Combust. Sci., 2008. **34**(4): p. 440-498.
2. Hébrard, É., et al., *Determining predictive uncertainties and global sensitivities for large parameter systems: A case study for n-butane oxidation.* Proceedings of Combustion Institute, 2014. http://dx.doi.org/10.1016/j.proci.2014.06.027.
3. Zádor, J., C.A. Taatjes, and R.X. Fernandes, *Kinetics of elementary reactions in low-temperature autoignition chemistry.* Prog. Energy Combust. Sci., 2010. **37**: p. 371-421.
4. Zhao, F., et al., eds. *Homogeneous Charge Compression Ignition (HCCI) Engines: Key Research and Development Issues*. 2003, Society of Automotive Engineers: Pittsburgh, PA. 600.
5. Adams, H., et al., *Color-Center Laser Spectroscopy of Transient Species Produced by Excimer-Laser Flash Photolysis.* J. Opt. Soc. Am. B, 1985. **2**(5): p. 776-780.
6. Hirota, E., *From High-Resolution Spectroscopy to Chemical Reactions.* Annu. Rev. Phys. Chem., 1991. **42**: p. 1-22.
7. Taatjes, C.A., *Time-resolved infrared absorption measurements of product formation in Cl atom reactions with alkenes and alkynes.* Int. Rev. Phys. Chem., 1999. **18**(3): p. 419-458.
8. Huang, H., et al., *New experiments and validated master-equation modeling for OH production in propyl + O_2 reactions* Proc. Combust. Inst., 2010. **33**: p. 293-299.
9. Dorn, H.-P., R. Neuroth, and A. Hofzumahaus, *Investigation of OH absorption cross sections of rotational transitions in the $A\ ^2\Sigma^+\ v' = 0 \leftarrow X\ ^2\Pi,\ v'' = 0$ band under atmospheric conditions: Implications for tropospheric long-path absorption measurements.* J. Geophys. Res. D, 1995. **100**(D4): p. 7397-7409.
10. Christophorou, L.G. and J.K. Olthoff, *Electron Interactions With Cl_2.* Journal of Physical and Chemical Reference Data, 1999. **28**(1): p. 131-169.
11. Baklanov, A.V. and L.N. Krasnoperov, *Oxalyl Chloride – A Clean Source of Chlorine Atoms for Kinetic Studies.* J. Phys. Chem. A, 2001. **105**: p. 97-103.
12. Wallington, T.J., P. Dagaut, and M.J. Kurylo, *Ultraviolet absorption cross sections and reaction kinetics and mechanisms for peroxy radicals in the gas phase.* Chem. Rev., 1992. **92**: p. 667-710.
13. Baasandorj, M., et al., *$(CH_3)_3COOH$ (tert-butyl hydroperoxide): OH reaction rate coefficients between 206 and 375 K and the OH photolysis quantum yield at 248 nm.* Phys. Chem. Chem. Phys., 2010. **12**: p. 12101-12111.
14. Rothman, L.S., et al., *The HITRAN 2004 molecular spectroscopic database.* J. Quant. Spectrosc. Radiat. Trans., 2005. **96**: p. 139-204.
15. Clifford, E.P., et al., *Infrared Frequency-Modulation Probing of Product Formation in Alkyl + O_2 Reactions: I. The Reaction of C_2H_5 with O_2 between 295 and 698 K.* J. Phys. Chem. A, 2000. **104**(49): p. 11549-11560.
16. Fink, E.H. and D.A. Ramsay, *High-resolution study of the $\tilde{A}^2A' \rightarrow X^2A''$ transition of HO_2: Analysis of the 000-000 band.* J. Mol. Spectrosc., 1997. **185**(2): p. 304-324.
17. DeSain, J.D., A.D. Ho, and C.A. Taatjes, *High Resolution Diode Laser Absorption Spectroscopy of the O-H Stretch Overtone Band (2,0,0) (0,0,0) of the HO_2 Radical.* J. Mol. Spectrosc., 2003. **219**: p. 163-169.
18. Jerome Thiebaud, Sabine Crunaire, and C. Fittschen, *Measurements of Line Strengths in the $2\nu_1$ Band of the HO_2 Radical Using Laser Photolysis/Continuous Wave Cavity Ring-Down Spectroscopy (cw-CRDS).* Journal of Physical Chemistry A, 2007. **111**(30): p. 6859-6966.
19. Zádor, J., et al., *The reaction of hydroxyethyl radicals with O_2: a theoretical analysis and experimental product study.* Proc. Combust. Inst., 2009. **32**: p. 271-277.
20. Welz, O., et al., *Unconventional Peroxy Chemistry in Alcohol Oxidation: The Water Elimination Pathway.* The Journal of Physical Chemistry Letters, 2013. **4**(3): p. 350-354.

21. Welz, O., et al., *Low-Temperature Combustion Chemistry of n-Butanol: Principal Oxidation Pathways of Hydroxybutyl Radicals.* The Journal of Physical Chemistry A, 2013. **117**(46): p. 11983-12001.
22. Brown, L.R., R.H. Hunt, and A.S. Pine, *Wavenumbers, Line Strengths, and Assignments in the Doppler-Limited Spectrum of Formaldehyde from 2700 to 3000 cm^{-1}.* Journal of Molecular Spectroscopy, 1979. **75**: p. 406-428.
23. Nelson, D.D., A. Schiffman, and D.J. Nesbitt, *The dipole moment function and vibrational transition intensities of OH.* The Journal of Chemical Physics, 1989. **90**(10): p. 5455-5465.
24. Nelson, D.D., et al., *$H+O_3$ Fourier- transform infrared emission and laser absorption studies of OH ($X^2\Pi$) radical: An experimental dipole moment function and state-to-state Einstein A coefficients.* The Journal of Chemical Physics, 1990. **93**(10): p. 7003-7019.
25. Nelson, D.D., et al., *Absolute infrared transition moments for open shell diatomics from J dependence of transition intensities: Application to OH.* The Journal of Chemical Physics, 1989. **90**(10): p. 5443-5454.
26. Schiffman, A. and D.J. Nesbitt, *Pressure broadening and collisional narrowing in OH(v=1 ← 0) rovibrational transitions with Ar, He, O_2, and N_2.* The Journal of Chemical Physics, 1994. **100**(4): p. 2677-2689.
27. Pilgrim, J.S., R.T. Jennings, and C.A. Taatjes, *Temperature Controlled Multiple Pass Absorption Cell for Gas Phase Chemical Kinetics Studies.* Rev. Sci. Instrum., 1997. **68**(4): p. 1875-1878.
28. Herriott, D., H. Kogelnik, and R. Kompfner, *Off-Axis Paths in Spherical Mirror Interferometers.* Appl. Opt., 1964. **3**: p. 523.
29. MELNIK, D.G., *TJ14: QUANTITATIVE ABSORPTION AND KINETIC STUDIES OF TRANSIENT SPECIES USING GAS PHASE OPTICAL CALORIMETRY*, in *2014 International Symposium on Molecular Spectroscopy*. 2014: University of Illinois, Urbana-Champaign.
30. Zádor, J., et al., *Directly measuring reaction kinetics of QOOH – a crucial but elusive intermediate in hydrocarbon autoignition.* Physical Chemistry Chemical Physics, 2013. **15**: p. 10753-10760.
31. Huang, H., A.J. Eskola, and C.A. Taatjes, *Pressure-Dependent I-Atom Yield in the Reaction of CH_2I with O_2 Shows a Remarkable Apparent Third-Body Efficiency for O_2.* Journal of Physical Chemistry Letters, 2012. **3**(22): p. 3399-3403.
32. Huang, H., et al., *Correction to "Pressure-Dependent I Atom Yield in the Reaction of CH_2I with O_2 Shows a Remarkable Apparent Third-Body Efficiency for O_2".* Journal of Physical Chemistry Letters, 2013. **4**: p. 3824-3824.
33. Baughcum, S.L. and S.R. Leone, *Photofragmentation infrared emission studies of vibrationally excited free radicals CH_3 and CH_2I.* Journal of Chemical Physics, 1980. **72**(12): p. 6531-6545.

Distribution

1	MS0899 Technical Library	9536 (electronic copy)


Sandia National Laboratories